

# Signatures of Inflowing Gas in Red Geyser Galaxies Hosting Radio Active Galactic Nuclei

Namrata Roy<sup>1</sup>, Kevin Bundy<sup>1,2</sup>, Kate H. R. Rubin<sup>3</sup>, Kate Rowlands<sup>4,5</sup>, Kyle Westfall<sup>1,2</sup>, Rogerio Riffel<sup>6,7</sup>, Dmitry Bizyaev<sup>8</sup>, David V. Stark<sup>9</sup>, Rogemar A. Riffel<sup>10,7</sup>, Ivan Lacerna<sup>11,12</sup>, Preethi Nair<sup>13</sup>, Xuanyi Wu<sup>14</sup>, and Niv Drory 15 Department of Astronomy and Astrophysics, University of California, 1156 High Street, Santa Cruz, CA 95064, USA; naroy@ucsc.edu <sup>2</sup> UCO/Lick Observatory, Department of Astronomy and Astrophysics, University of California, 1156 High Street, Santa Cruz, CA 95064, USA San Diego State University, Department of Astronomy, San Diego, CA 92182, USA AURA for ESA, Space Telescope Science Institute, Baltimore, MD, USA <sup>5</sup> Johns Hopkins University, Department of Physics and Astronomy, Baltimore, MD 21218, USA <sup>6</sup> Departamento de Astronomia, Instituto de Física, Universidade Federal do Rio Grande do Sul, CP 15051, 91501-970, Porto Alegre, RS, Brazil Laboratório Interinstitucional de e-Astronomia—LIneA, Rua Gal. José Cristino 77, Rio de Janeiro, RJ - 20921-400, Brazil Apache Point Observatory, P.O. Box 59, Sunspot, NM 88349, USA Haverford College, Department of Physics and Astronomy, 370 Lancaster Avenue, Haverford, PA 19041, USA Departamento de Física, CCNE, Universidade Federal de Santa Maria, 97105-900, Santa Maria, RS, Brazil Instituto de Astronomía y Ciencias Planetarias, Universidad de Atacama, Copayapu 485, Copiapó, Chile <sup>12</sup> Millennium Institute of Astrophysics, Nuncio Monsenor Sotero Sanz 100, Office 104, Providencia, Santiago, Chile University of Alabama, Department of Physics and Astronomy, Tuscaloosa, AL 35487, USA University of Alabama, Department of Trysics and Tings 100084, People's Republic of China Tsinghua University, Department of Astronomy, Beijing 100084, People's Republic of China (1971) 15 McDonald Observatory, The University of Texas at Austin, 1 University Station, Austin, TX 78712, USA Received 2021 April 13; revised 2021 June 25; accepted 2021 June 27; published 2021 October 5

#### Abstract

We study cool neutral gas traced by NaD absorption in 140 local (z < 0.1) early-type red geyser galaxies. These galaxies show unique signatures in spatially resolved strong line emission maps that have been interpreted as large-scale active galactic nucleus—driven ionized winds. To investigate the possible fuel source for these winds, we examine the abundance and kinematics of cool gas ( $T \sim 100-1000 \, \mathrm{K}$ ) inferred from Na I D absorption in red geysers and matched control samples drawn from the Sloan Digital Sky Survey IV Mapping Nearby Galaxies at Apache Point Observatory survey. We find that red geysers host greater amounts of NaD-associated material. Substantial cool gas components are detected in more than 50% of red geysers (compared to 25% of the control sample) going up to 78% for radio-detected red geysers. Our key result is that cool gas in red geysers is predominantly infalling. Among our 30 radio-detected red geysers, 86% show receding NaD absorption velocities (with respect to the systemic velocity) between 40 and 50 km s<sup>-1</sup>. We verify this result by stacking NaD profiles across each sample, which confirms the presence of infalling NaD velocities within red geysers ( $\sim 40 \, \mathrm{km \, s^{-1}}$ ) with no velocity offsets detected in the control samples. Interpreting our observations as signatures of inflowing cool neutral clouds, we derive an approximate mass inflow rate of  $\dot{M}_{\mathrm{in}} \sim 0.1 M_{\odot} \, \mathrm{yr^{-1}}$ , similar to that expected from minor merging and internal recycling. Some red geysers show much higher rates ( $\dot{M}_{\mathrm{in}} \sim 5 M_{\odot} \, \mathrm{yr^{-1}}$ ), which may indicate an ongoing accretion event.

*Unified Astronomy Thesaurus concepts:* Galaxy evolution (594); Galaxy quenching (2040); AGN host galaxies (2017); Galactic winds (572)

# 1. Introduction

Low-redshift (z < 0.1) integral field unit (IFU) spectroscopy from the Sloan Digital Sky Survey IV (SDSS-IV) Mapping Nearby Galaxies at Apache Point Observatory (MaNGA) survey (Bundy et al. 2015) has revealed a population of moderate-mass (log  $M_{\star}/M_{\odot} \sim 10.5$ ) passive red galaxies (NUV - r > 5), known as "red geysers" (Cheung et al. 2016; Roy et al. 2018). These galaxies possess unique emission and kinematic properties that may be signatures of galactic-scale ( $\sim$ 10 kpc), centrally driven outflows (Cheung et al. 2016; Roy et al. 2021). The lack of any detectable star formation (average log SFR  $(M_{\odot} \text{ yr}^{-1}) < -2$ , using GALEX+SDSS+WISE from Salim et al. 2016; see Figure 1), the association with lowluminosity radio-mode active galactic nuclei (AGNs; Roy et al. 2018), and the relatively high occurrence rate on the red sequence (5%–10%; see Cheung et al. 2016) make red geysers a candidate for supplying "maintenance (or radio) mode" feedback by low-luminosity AGNs. While such a feedback process has been widely proposed and studied as a way to suppress star formation at late times (Binney & Tabor 1995;

Ciotti & Ostriker 2001; Croton et al. 2006; Bower et al. 2006; Faber et al. 2007; Ciotti et al. 2010; Yuan & Narayan 2014), direct observational evidence in typical quiescent galaxies has remained elusive.

Red geysers are characterized by a distinctive bisymmetric pattern in spatially resolved equivalent width (EW) maps of strong emission lines (H, [N II], and [O II]). These features extend to ~10 kpc, up to the edge of the MaNGA fiber bundle. The emission-line flux distributions are also widespread and significantly elevated (~5–10 times) along the bisymmetric feature. The observed gas is possibly ionized by postasymptotic giant branch stars with some contribution from shocks, as evident from the combination of LI(N)ER and Seyfert-like line ratios in spatially resolved Baldwin–Phillips–Terlevich (BPT; Baldwin et al. 1981) diagrams in these galaxies (Cheung et al. 2016; Roy et al. 2021). This enhanced emission roughly aligns with the gas kinematic major axis but is strongly misaligned with the stellar velocity gradient.

Accreted gas disks in early-type galaxies (Chen et al. 2016; Lagos et al. 2014, 2015; Sarzi et al. 2006; Davis et al. 2013;

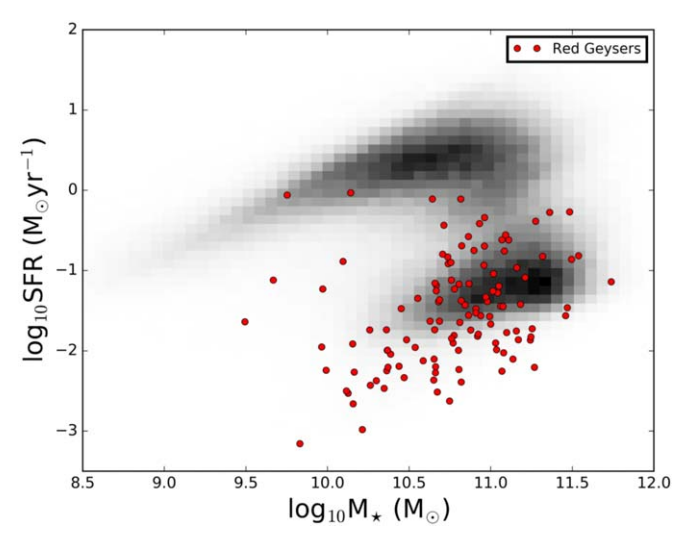


**Figure 1.** This figure shows the log SFR vs. the log  $M_{\star}$  as obtained from the GALEX+SDSS+WISE catalog of Salim et al. (2016). The gray 2D histogram shows all the MaNGA galaxies in the catalog with 0.01 < z < 0.1. The red circles signify the red geyser galaxies. Most of the galaxies in our chosen geyser sample have a low log SFR value, with an average of  $\sim 0.01 M_{\odot} \text{ yr}^{-1}$ .

Bryant et al. 2019; Duckworth et al. 2020) can produce similar misaligned stellar and gas velocity fields so it is important to test the hypothesis that red geysers signal the presence of outflows. Cheung et al. (2016) presented detailed dynamical modeling and concluded that the observed ionized gas velocities in the prototypical red geyser were too high to be in gravitationally bound orbits. More recently, our group used the Keck Echellette Spectrograph and Imager to obtain higher spectral resolution observations ( $R \sim 8000$  compared to  $R \sim 2000$  in MaNGA) of two representative red geysers to find a systematic variation in the asymmetry of the emissionline profiles with the radius (Roy et al. 2021). The observed magnitude and nature of the asymmetry along with the increased velocity dispersion (exceeding  $\sim 230 \, \mathrm{km \, s^{-1}}$ ) are consistent with line-of-sight projections through a broad conical outflow. The alternative scenario of a puffy, rotating gas disk does not fit the data.

An additional set of tests involve the mechanism driving the putative wind. Riffel et al. (2019) studied the nuclear region of the prototypical red geyser in Cheung et al. (2016) with the Gemini Multi-object Spectrograph. Comparing the emissionline flux distributions and gas kinematics from the inner parts (within 1") with those of the outer regions (5" away from the center), they concluded that the observed red geyser shows signatures of precession. Roy et al. (2018), meanwhile, used the Very Large Array (VLA) Faint Images of the Radio Sky at Twenty-centimeters (FIRST) survey to measure significantly higher ( $>5\sigma$ ) radio continuum flux in stacked red geyser samples and a three times higher radio detection rate compared to control samples. The study concluded that red geysers host low-luminosity radio AGNs ( $L_{1.4\text{GHz}} \sim 10^{22} - 10^{23} \, \text{W Hz}^{-1}$ ) with radiatively inefficient accretion (Eddington-scaled accretion rate  $\lambda \sim 10^{-4}$ ). These AGNs are energetically capable, however, of driving subrelativistic winds consistent with the MaNGA observations.

What is the fuel source for this AGN activity? The presence of warm ionized gas suggests the possibility that red geysers also host cooler gas reservoirs in the interstellar medium (ISM). Cool gas in the form of outflows is routinely observed in

ultraluminous IR galaxies, star-forming galaxies, and post-starburst galaxies (Martin et al. 2005; Weiner et al. 2009; Chen et al. 2010; Coil et al. 2011; Rubin et al. 2012, 2014; Alatalo et al. 2016; Cazzoli et al. 2016; Yesuf et al. 2017; Roberts-Borsani & Saintonge 2019; Rupke 2018; Veilleux et al. 2020). Indeed, Cheung et al. (2016) studied signatures of cool material traced by NaD absorption in their prototypical red geyser. With a mass estimated at  $M_{\rm cool} \sim 10^8 \, M_{\odot}$ , the NaD component occupied one side of the galaxy, kinematically and spatially distinct from the ionized gas and apparently inflowing at  $\sim 60 \, {\rm km \, s^{-1}}$  toward the center. An idealized merger simulation run by these authors suggests that the cool gas was being accreted from a companion galaxy.

Detecting gaseous inflows across the galaxy population in general has garnered significant attention, but definitive inflow signatures have been hard to detect (although see Sato et al. 2009; Krug et al. 2010; Putman et al. 2012; Rubin et al. 2012; Zheng et al. 2017; Sarzi et al. 2016). The advent of IFU surveys is revolutionizing this field with the measurement of spatially resolved absorption line kinematics in large samples of galaxies (Rupke et al. 2021; K. Rowlands et al. 2021, in preparation). Here, the kinematics of cool gas are computed by estimating the Doppler shifts of suitable lines with respect to the systemic velocity after carefully accounting for the stellar continuum (the down-the-barrel technique; Roberts-Borsani & Saintonge 2019). This method involves probing the gas lying in front of the galaxy, with the continuum arising due to illumination by the background stellar light of the galaxy. Redshifted absorption indicates inflows, i.e., the motion of the gas toward the galaxy (or away from the observer along the line of sight). Similarly, a blueshifted component suggests outflows. Different tracers are available in rest-frame UV or optical wavelengths (e.g., Fe II  $\lambda\lambda 2586$ , 2600; Mg II  $\lambda\lambda 2796$ , 2803; and Na I D  $\lambda\lambda$ 5891, 5897; Chen et al. 2010; Rubin et al. 2012, 2014; Rupke 2018; Veilleux et al. 2020). In this work we use the resonant Na I absorption doublet at 5891 Å and 5897 Å (referred to as NaD), which traces cool ( $T \sim 100-1000$  K), metalenriched gas.

An important aspect of measuring NaD-associated gas kinematics correctly is subtracting the stellar continuum with an appropriate accuracy. This is especially important in earlytype galaxies, since the evolved K-M-type stars present throughout the galaxy can contribute a significant fraction to sodium absorption in the spectrum, thus contaminating the signal from the ISM. There exist several stellar population model libraries (theoretical and empirical) that can be used to estimate the stellar component of NaD absorption generally within a variation of  $\sim 10\%$ –30%. This difference in the continuum estimate due to the specific choice of stellar model can affect the estimated properties of the ISM gas. Spatially resolved spectra from MaNGA can aid this process significantly by revealing irregularities in the 2D morphology of the NaD absorption. When these spatial irregularities have no correspondence to the stellar velocity and the surface brightness distribution, we can be more confident that they are associated with the ISM.

The goal of this work is to address how frequent cool gas as traced by NaD is found within the red geyser sample and whether these cooler gas reservoirs are associated with inflows toward the center, similar to the prototypical red geyser, or with the outflowing wind triggered by the AGN. We will also study if there exists any possible correlation between radio properties

and the presence of cool gas, by conducting our analyses on samples split by radio detection. We analyze the spatially resolved, globally integrated, and stacked kinematics of NaD from the red geyser sample and compare them with those of a matched control sample. We find that the red geysers, especially those that were detected in FIRST, have greater NaD EWs on average and 78% of the sample show detectable ISM gas over a projected spatial extent >5 kpc. This fraction is many times higher than those for the radio-detected control (41%) and non-radio-detected control (25%) galaxies. The kinematics is observed to be redshifted on average ( $\sim$ 40–50 km s<sup>-1</sup>) in  $\sim$ 86% of radio-detected red geysers, implying that most of the gas is inflowing into the galaxy possibly fueling the central active black hole.

Section 2.1 gives a brief overview of the optical data from MaNGA that we have used in this work and in Section 2.2 we describe the sample selection process of the red geyser and control galaxy samples from the MaNGA quiescent population. The technical details of the stellar continuum modeling, EW estimation, absorption line fitting, and kinematics calculation are presented in Sections 3.1, 3.2, and 3.3. The results of the analyses are described in Section 4 and the implications and concluding remarks are discussed in Sections 5 and 6. Throughout this paper, we assume a flat cosmological model with  $H_0 = 70 \text{ km s}^{-1} \text{ Mpc}^{-1}$ ,  $\Omega_{\rm m} = 0.30$ , and  $\Omega_{\Lambda} = 0.70$ , and all magnitudes are given in the AB magnitude system.

# 2. Data Acquisition and Sample Definitions

# 2.1. The MaNGA Survey

We use data primarily from the recently completed SDSS-IV MaNGA survey (Blanton et al. 2017; Bundy et al. 2015; Drory et al. 2015; Law et al. 2015; Yan et al. 2016; Albareti et al. 2017). MaNGA is an integral field spectroscopic survey that provides spatially resolved spectroscopy for nearby galaxies  $(z \sim 0.03)$  with an effective spatial resolution of 2.5" (FWHM). The MaNGA survey uses the SDSS 2.5 m telescope in spectroscopic mode (Gunn et al. 2006) and the two dualchannel BOSS spectrographs (Smee et al. 2013), which provide continuous wavelength coverage from the near-UV to the near-IR: 3600-10000 Å. The spectral resolution varies from  $R \sim 1400$  at  $4000 \,\text{Å}$  to  $R \sim 2600$  at  $9000 \,\text{Å}$ . An r-band signal-to-noise ratio (S/N) of  $4-8 \,\text{Å}^{-1}$  is achieved in the outskirts (i.e., 1-2 R<sub>e</sub>) of target galaxies with an integration time of approximately 3 hr. MaNGA has observed more than 10,000 galaxies with  $\log (M_*/M_{\odot}) \gtrsim 9$  across  $\sim 2700 \deg^2$ over its 6 yr duration. In order to balance radial coverage versus spatial resolution, MaNGA observes two-thirds of its galaxy sample to  $\sim 1.5 R_e$  and one-third to  $2.5 R_e$ . The MaNGA target selection is described in detail in Wake et al. (2017).

The raw data are processed with the MaNGA Data Reduction Pipeline (Law et al. 2016). An individual row-by-row algorithm is used to extract the fiber flux and derive inverse variance spectra from each exposure, which are then wavelength-calibrated, flat-fielded, and sky-subtracted. We use a MaNGA sample and data products drawn from MaNGA Product Launch 9 (MPL-9) and Data Release 16 (Ahumada et al. 2020). We use spectral measurements and other analyses carried out by the MaNGA Data Analysis Pipeline (DAP), specifically version 2.3.0. The data we use here are based on DAP analysis of each spaxel in the MaNGA data cubes. The DAP first fits the stellar continuum of each spaxel to determine

the stellar kinematics using the penalized pixel-fitting algorithm pPXF (Cappellari & Emsellem 2004; Cappellari 2017) and templates based on the MILES stellar library (Falcón-Barroso et al. 2011). The templates are a hierarchically clustered distillation of the full MILES stellar library into 49 templates. This small set of templates provide statistically equivalent fits to those that use the full library of 985 spectra in the MILES stellar library. The emission-line regions are masked during this fit. The DAP then subtracts the result of the stellar continuum modeling to provide a (nearly) continuum-free spectrum that is used to fit the nebular emission lines. This version of the DAP treats each line independently, fitting each for its flux, Doppler shift, and width, assuming a Gaussian profile shape. The final output from the DAP is gas and stellar kinematics, emissionline properties, and stellar absorption indices. All spatially resolved 2D maps shown in the paper are outputs from the DAP with a hybrid binning scheme. An overview of the DAP used for Data Release 15 and its products is presented by Westfall et al. (2019), and assessments of its emission-line fitting approach are described by Belfiore et al. (2019).

We use ancillary data drawn from the NASA–Sloan Atlas<sup>16</sup> (NSA) catalog, which reanalyzes images and derives morphological parameters for local galaxies observed in SDSS imaging. It compiles spectroscopic redshifts, UV photometry (from the Galaxy Evolution Explorer (GALEX); Martin et al. 2005), stellar masses, and structural parameters. We have specifically used spectroscopic redshifts and stellar masses from the NSA catalog.

### 2.2. Sample Definitions

Red geysers are early-type galaxies lying in the red sequence (NUV-r>5) that have little or no ongoing star formation activity. Figure 1 shows the star formation rates (SFRs) of the red geyser sample (red circles) compared to all MaNGA galaxies (gray) from the Salim et al. (2016) catalog. This catalog derived SFRs from UV/optical spectral energy distribution fitting with additional constraints from mid-IR data using GALEX+SDSS+WISE. The typical value of the SFR for the red geysers is  $\sim 0.01~M_{\odot}~\rm yr^{-1}$ . The sample of red geysers used here is derived from MPL-9 and consists of 140 galaxies, which account for  $\approx 6\%$ –8% of the local quiescent galaxy population observed by MaNGA. The red geyser sample is visually selected based on the characteristic features described in detail in Cheung et al. (2016), Roy et al. (2018), and Roy et al. (2021). They are briefly outlined below:

- 1. Spheroidal galaxies with no disk component as observed by SDSS and with low SFRs
- 2. Bisymmetric feature in spatially resolved EW map of strong emission lines like  $H\alpha$ , [N II], and [O III]
- 3. Rough alignment of the bisymmetric feature with the ionized gas kinematic axis, but misalignment with the stellar kinematic axis
- 4. High spatially resolved gas velocity values (typically reaching a maximum of  $\pm 300 \, \mathrm{km \, s^{-1}}$ ) that are greater than the stellar velocity values by at least a factor of 4–5
- 5. High gas velocity dispersion values, reaching  $\sim$ 220–250 km s<sup>-1</sup> in distinct parts of the galaxy
- 6. Predominantly showing LINER or Seyfert-type line ratios in spatially resolved BPT diagrams

<sup>16</sup> http://www.nsatlas.org

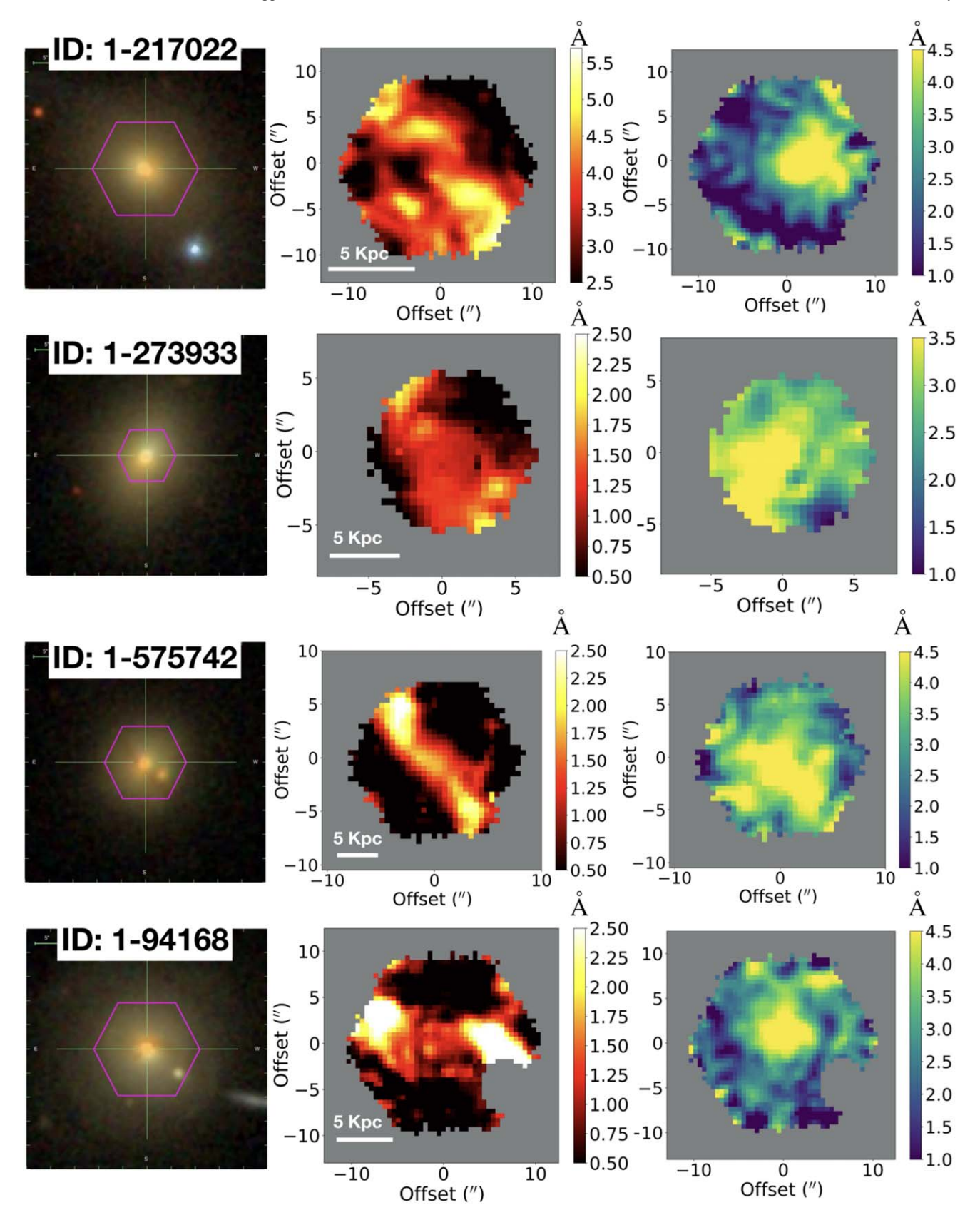


Figure 2. The spatially resolved emission and absorption line properties of four example red geysers (MaNGA ID: 1-217022, 1-273933, 1-575742, and 1-94168) from SDSS-IV MaNGA. The left panels show optical images of the galaxies from SDSS with the MaNGA IFU overlaid in magenta. The on-sky diameters of the IFU fibers shown here range from 12'' to 22'' corresponding to physical sizes of roughly 10-20 kpc. The middle panels show the H $\alpha$  EW maps (observed-frame units of angstroms) showing the signature bisymmetric pattern identifying the red geyser class, and the right panels show the EW map of NaD absorption (in angstroms), which includes both the stellar and cool ISM gas components.

Four example red geysers are shown in Figure 2. Optical images (left panels) from SDSS show the spheroidal morphology typical of these galaxies. The middle panels show the characteristic bisymmetric feature in the H EW map. The right panels show the NaD EW map obtained using the MaNGA DAP (see Section 10 in Westfall et al. 2019 for details). The DAP performs spectral index measurements after first subtracting the best-fit emission-line model from the observed spectrum. It does not perform any stellar continuum subtraction on the NaD feature; hence the observed EW shows the presence of both the stellar and the ISM component. However the NaD maps show a highly anisotropic and clumpy spatial morphology, indicating that a major portion of the observed NaD absorption is likely contributed by ISM gas. We also find that the regions with large NaD EWs are spatially offset from the bisymmetric feature observed in the H map suggesting the presence of multiphase gas components tracing different activities in these galaxies.

Roy et al. (2018) cross-matched the red geyser sample with the VLA-FIRST catalog to identify the radio-detected red geysers. For the latest sample from MPL-9, we have an updated list of radio-detected red geysers consisting of 30 galaxies.

We construct a control sample of spheroidal quiescent galaxies that are matched in global properties, namely stellar mass, color, redshift, and axis ratio, but do not show resolved geyser-like features as described previously. For each red geyser, we match up to four quiescent galaxies (having NUV - r > 5) with the following criteria:

- 1.  $\log M_{\star, \rm red~geyser}/M_{\star, \rm control} < 0.2~{\rm dex}$ 2.  $z_{\rm red~geyser} z_{\rm control} < 0.01$ 3.  $b/a_{\rm red~geyser} b/a_{\rm control} < 0.1$

where  $M_{\star}$  is the stellar mass, z is the spectroscopic redshift, and b/a is the axis ratio from the NSA catalog. This technique results in 458 unique control galaxies with 65 of them detected in FIRST. These constitute the radio-detected control sample.

# 3. Data Analysis

# 3.1. Stellar Continuum Fitting

The sodium doublet feature can arise from photospheric transitions in evolved cool stars, as well as from cool neutral gas in the ISM. Since our samples consist of red and quiescent galaxies with evolved stellar populations, the K-M-type stars throughout the galaxy are likely to make up a major fraction of the spectral NaD profile (Jacoby et al. 1984; Tyson & Rich 1991) with the residual absorption attributed to the ISM component. On the other hand, since the primary contribution in the magnesium triplet Mg II  $\lambda\lambda\lambda5167$ , 5173, 5184 (Mg b) absorption is from the stars, studies of star-forming galaxies have found a linear relation between the EWs of Mg b and NaD from the stellar component alone (Alatalo et al. 2016). In spite of the observed scatter around the empirical relation in Alatalo et al. (2016), any enhancement in NaD as compared to Mg b beyond the relation likely indicates an ISM contribution.

Figure 3 (upper panel) compares the EWs of the NaD and Mg b of red geysers (cyan and magenta squares, representing radio-detected and non-radio-detected galaxies from the FIRST survey, respectively) and the control sample (gray circles), obtained by averaging the EWs measured by the MaNGA DAP (which include NaD absorption from both the stellar and ISM components) over all spaxels within one effective radius. The

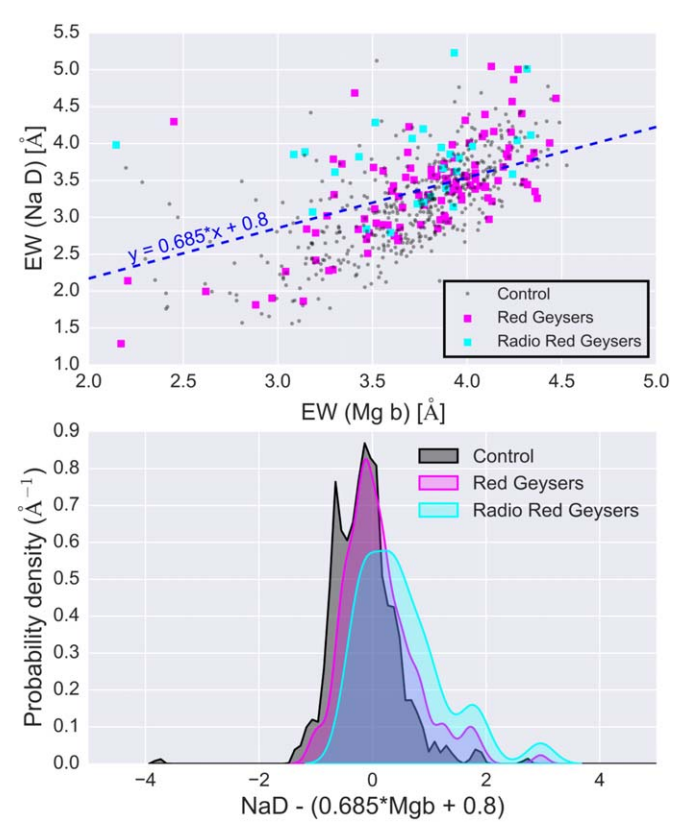
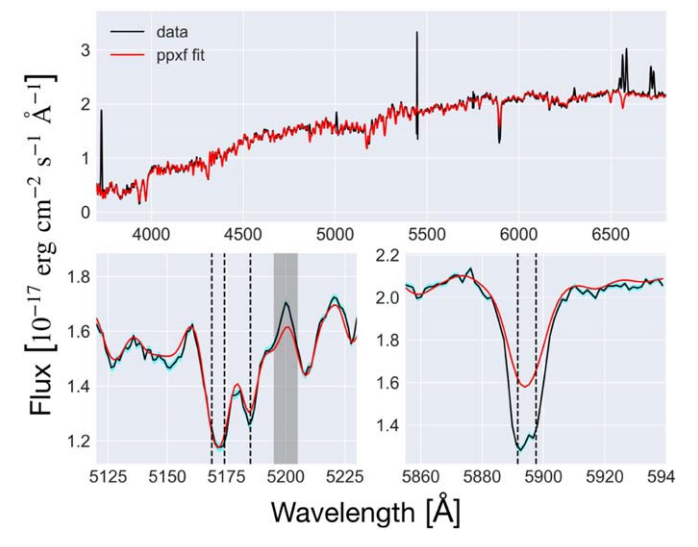


Figure 3. [Upper panel] EW(NaD) vs. EW(Mg b) of the red geysers (magenta squares) and control sample (gray circles). The FIRST-detected radio red geysers are colored cyan. The blue dashed line represents the empirical relation from the stellar component only found in Alatalo et al. (2016) for star-forming galaxies. Any object above the relation is expected to have a dominant ISM contribution in NaD. [Lower panel] Probability density functions for the Na I D EWs, measured with respect to the mean Alatalo et al. (2016) relation:  $EW(NaD) = 0.685^*EW(Mg b) + 0.8$  (indicated by the blue dashed line in the upper panel) for the different subsamples. The radio-detected red geysers (cyan) show a clear departure from the other two distributions, with a large fraction of objects showing excess NaD as compared to their Mg b.

figure shows that a large fraction of the galaxies in the radiodetected red geyser sample have a considerable excess in NaD lying above the Alatalo et al. (2016) empirical relation (blue dashed line).

This is further confirmed by the lower panel in Figure 3, which shows the probability density function of the deviation of the NaD EW distribution with respect to the Alatalo et al. (2016) relation. We find that a large fraction of radio-detected red geysers show an excess amount of NaD, as indicated by the clear positive wing in the distribution, as compared to the other two samples. In fact, 75% of the radio red geyser sample lie above the relation, compared to 51% of the non-radio-detected red geysers and only 32% of the control sample. This indicates an elevated abundance of cool gas within radio-detected red geysers and a possible correlation with the presence of radiodetected AGNs, which we will return to below.

It is to be noted from Figure 3 that there exists a notable amount of NaD deficit at low Mg b particularly for the control galaxies. This is likely caused by the infilling of the resonant NaD emission line, which has been previously detected in integrated, stacked, and spatially resolved NaD spectra (Alatalo et al. 2016; Chen et al. 2010; Rupke et al. 2021). The nonradio-detected red geysers, on the other hand, show a roughly equal fraction of galaxies with NaD deficit (at low Mg b) and



**Figure 4.** The top panel shows an example MaNGA spectrum in black. The best-fit stellar continuum obtained from the pPXF fit using MIUSCAT stellar population models, as described in Section 3.1, is overplotted in red. The results of the continuum fit around the magnesium triplet (Mg b) and sodium doublet (NaD) absorption lines are shown in the left and right subplots in the bottom panel, respectively. The  $1\sigma$  errors in the observed spectra are shown in the bottom panels in cyan. The gray shaded region in the lower left panel highlights the [N I] emission line at 5200 Å.

excess (at high Mg b) with a rather symmetric distribution overall.

The next step is to accurately model out the stellar continuum contribution to the NaD absorption in order to extract the residual gaseous component. First, we mask spaxels with low or no spectral coverage, low S/N, or foreground stars, unreliable fits, or noisy observations as flagged by MaNGA under the mask-bit names NOCOV, LOWCOV, FORESTAR, UNRELIABLE, and DONOTUSE. Then, following K. Rubin et al. (2021 in preparation), we bin and stack the spectra in  $2^{\prime\prime}\times2^{\prime\prime}$  spatial bins (or spaxels) to acquire a good continuum S/N (>10 per dispersion element) per bin throughout the galaxy.

We then fit the stellar continuum for each spatial bin with pPXF (Cappellari & Emsellem 2004; Cappellari 2017), which fits a linear combination of simple stellar population (SSP) model templates. Here, we make use of the MIUSCAT SSP (Vazdekis et al. 2012), although a detailed comparison with other SSP models is presented later. Strong emission line regions are masked during the fit. We also mask the region around the NaD transition, as we assume that the doublet is a result of stellar plus ISM contributions and hence should not be fit by the model. We also mask the red half of the He I emission line at 5875.67 Å, which is close enough to the NaD line that it could affect the residual profile. An example spectrum and its continuum fit are shown in Figure 4. The stellar continuum model shows a satisfactory fit, with minimal residuals around Mg b and an excess around NaD, which hint at the presence of ISM gas.

To remove the stellar continuum and isolate the ISM component, the spectrum in each bin is divided by the best corresponding continuum fit. We additionally fit a first-order polynomial to the continuum-normalized spectrum in the wavelength range immediately (20 Å) blueward and redward of the NaD profile and divide the residual by the polynomial fit.

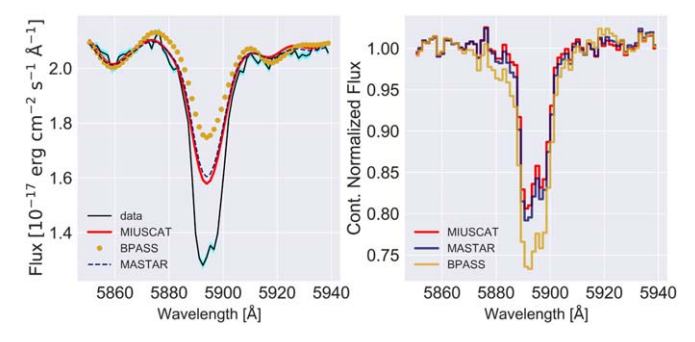


**Figure 5.** The left panel shows the modeled stellar continuum obtained by using three different stellar population models (MIUSCAT, BPASS, and MaStar) in different colors and line styles, overplotted on the observed NaD absorption spectra in black. The  $1\sigma$  error of the observed NaD spectrum is shown in cyan. The right panel shows the corresponding continuum-normalized residual NaD indicating a contribution from the ISM.

This is to account for any systematic errors in the continuum fitting that might give rise to artificial residuals.

We now examine the robustness of our stellar continuum modeling to the assumed stellar library. We repeat the above continuum fitting process for 10 galaxies in each of the red geyser and control samples across every spatial bin using two additional libraries, namely MaStar (Yan et al. 2019), an empirical library constructed using the MaNGA instrumentation, and BPASS (Eldridge et al. 2017), a theoretical template library. The BPASS SSP models are drawn from the v2.2.1 release, which adopted the default BPASS initial mass function. The SSPs over a range of log ages (in gigayears) of -1.2 to 1.1, with stellar metallicity mass fractions Z = 0.008, 0.02, and 0.03, are included. The BPASS fitting will be described in full in K. Parker et al. (2021, in preparation).

An example of the variation of the stellar contribution owing to the different stellar population models is shown in the left panel of Figure 5. The different colors indicate the SSPs used to construct the stellar model. The right panel shows the continuum-normalized NaD spectra using the same SSPs. We find that the fractional differences in NaD EW of the continuum-normalized spectra, computed using the MaStar and MIUSCAT models, range between 5% and 15% in the 10 red geyser galaxies studied. However, the BPASS model can change the estimated EW by about 25%-30%, as compared to the other two models. BPASS is the result of combining theoretical model spectra with as few empirical inputs as possible. Hence it differs substantially from the two other stellar models (MIUSCAT and MaStar), which are based on empirical libraries. Preliminary work has revealed that the BPASS continuum model may be underpredicting the amount of NaD coming from stellar atmospheres (K. Parker et al. 2021, in preparation). On the other hand, the stellar models from MIUSCAT and the MaStar models, drawing on empirical libraries, likely contain some interstellar Na I absorption from the Milky Way, overpredicting NaD absorption from stars. Thus, the three models are different and are shown to explore a broad range of parameter space in stellar continuum modeling and their effect in our analyses.

Although the EW value of the continuum-normalized NaD spectra changes owing to the different stellar models, the velocity difference is negligible ( $<5 \,\mathrm{km \, s^{-1}}$ ), as shown by the example in Figure 5. Among the three libraries we test, we use

<sup>&</sup>lt;sup>17</sup> These are freely available at https://bpass.auckland.ac.nz/9.html.

the MIUSCAT SSPs in what follows because this particular set of models yields the most conservative (lowest) value of inferred NaD ISM contribution.

### 3.2. EW Calculation

Once the spectrum is continuum-normalized, the strength of the NaD absorption arising from the ISM is quantified by the EW. The EW is measured as follows:

$$W = h_{\lambda} \sum_{i=1}^{M} \left[ 1 - \frac{F_j}{F_c} \right] \tag{1}$$

where  $h_{\lambda}$  denotes the dispersion in wavelength in angstroms per pixel; M is the number of individual pixels that together constitute the desired wavelength interval, which includes the NaD absorption feature and 20 Å immediately blueward and redward of it; and  $F_j/F_c$  is the continuum-normalized flux for each of those pixels.

# 3.3. NaD Line Fitting Using Bayesian Inference

After continuum-normalizing the spectra as discussed in Section 3.1, we want to determine the kinematics of the neutral gas present in our galaxy samples. We perform a "detection" test for every spaxel to determine the significance of the ISM component in the NaD spectra with the following criteria:

- 1. The depth of the absorption trough in the residual spectra must be at least  $\sim 10\%$  of the continuum level.
- 2. The EW measured from the residual ISM component must be  $>0.3\,\text{Å}$ .
- 3. The S/N of each spectrum must be >10 per dispersion element.

The primary reason behind taking such restrictive criteria is to prevent biases from low-S/N spectra with extremely small inferred residuals, which would provide inaccurate kinematic estimates from erroneous model fits. As discussed later, an input spectrum with S/N < 10 gives an error of up to  $\sim\!20~{\rm km~s^{-1}}$  in measured velocities, which can be marginally close to the observed velocity amplitudes we wish to investigate. Requiring spectra with S/N > 10 ensures that the velocity errors remain within acceptable limits.

The NaD spectral features in the spaxels that satisfy all the requirements are then modeled with an analytical function (Rupke et al. 2005), which takes the following form:

$$I(\lambda) = 1 - C_f + C_f \times e^{-\tau_B(\lambda) - \tau_R(\lambda)}$$
 (2)

where  $C_{\rm f}$  is the velocity-independent covering factor, and  $\tau_{\rm B}(\lambda)$  and  $\tau_{\rm R}(\lambda)$  are the optical depths of the Na I  $\lambda$ 5891 and Na I  $\lambda$ 5897 (vacuum wavelength) lines, respectively. The optical depth of the line,  $\tau(\lambda)$ , can be expressed as

$$\tau(\lambda) = \tau_0 \times e^{-(\lambda - \lambda_0 + \Delta \lambda_{\text{offset}})^2 / ((\lambda_0 + \Delta \lambda_{\text{offset}}) b_D / c)^2}$$
 (3)

where  $\tau_0$  and  $\lambda_0$  are the central optical depth and central wavelength of each line component, respectively,  $b_{\rm D}$  is the Doppler line width, and c is the speed of light. The wavelength offset is converted from a velocity offset, given by  $\Delta \lambda_{\rm offset} = \Delta v \lambda_0/c$ . For NaD,  $\tau_{\rm 0,B}/\tau_{\rm 0,R} = 2$ . The optical depth parameter can be derived from the column density of sodium

described as

$$N(\text{Na I}) = \frac{\tau_0 b}{1.497 \times 10^{-15} \lambda_0 f}$$
 (4)

where  $\lambda_0$  and f are the rest-frame wavelength (vacuum) and oscillator strength, respectively. Throughout this study we assume  $\lambda_0 = 5897.55$  Å and f = 0.318 (Morton 1991).

The absorption feature is fitted here using a single kinematic component. Fitting the neutral gas absorption with one component is certainly an oversimplification in a scenario where contributions from more than one gas cloud along the line of sight are embedded within a single line profile. However, this approach allows us to characterize the global kinematics obtained from the data. The absorption model is convolved with MaNGA's instrumental resolution (~65 km s<sup>-1</sup>) before the fit is performed.

In order to explore possible degeneracies, obtain unbiased fits, and estimate the errors, we wrap our fitting procedure in a Bayesian inference approach using the dynamical nested sampling algorithm (Higson et al. 2019) as implemented in the Python package *dynesty* (Speagle 2020). Nested sampling (Skilling 2006, 2004) estimates both the Bayesian evidence and posterior distributions in an iterative fashion until the convergence criteria are met. The method has the flexibility to sample from complex, multimodal distributions using adaptive sampling to maximize the accuracy and efficiency of the fitting process. The greater flexibility and the ability to compute Bayesian evidence (Z) on top of posteriors are advantages over traditional Markov Chain Monte Carlo (MCMC) methods. The default stopping criterion for dynesty is used in our analyses with no limitation on the maximum number of iterations. We have set reasonable priors in our MCMC fitting routine: the line width is constrained within  $\pm 100 \,\mathrm{km \, s^{-1}}$  of the stellar line width obtained from the continuum model and the limits on the allowed velocity are set at  $\pm 500 \,\mathrm{km \, s}^{-1}$ . The covering fraction takes values between 0 and 1. No constraints are placed on the column density parameter. Figure 6 shows two examples of model fits applied to two different spatial bins of a red geyser (MaNGA ID: 1-217022). The residuals vary from 2% to 5%, indicating an acceptable model fit.

For each input spectrum, our procedure delivers estimates of the column density, velocity, line width, and covering fraction. The best-fit velocity with respect to the systemic velocity is assigned to the kinematics of the neutral ISM at that location.

As a key aspect of this paper is a characterization of the global NaD kinematics in our red geyser sample, it is important to test the robustness of our velocity measurements to systematic biases. Such biases might be expected: we are fitting an asymmetric absorption doublet model to the spectral residual obtained after subtracting a broadened and possibly offset version (from the stellar continuum) of a similar doublet model.

We begin by generating synthetic stellar NaD absorption spectra assuming a Gaussian stellar velocity profile of the amplitude and width observed from the stellar continuum model of our example galaxy with MaNGA ID 1-217022. The mean of the Gaussian is set to the systemic velocity of the galaxy. We simulate the ISM component using the doublet absorption model of Rupke et al. (2005) with average values set for each parameter, namely, column density =  $2.9 \times 10^{13} \, \mathrm{cm}^{-2}$ , line width  $(\sigma) = 150 \, \mathrm{km \, s}^{-1}$ , and covering

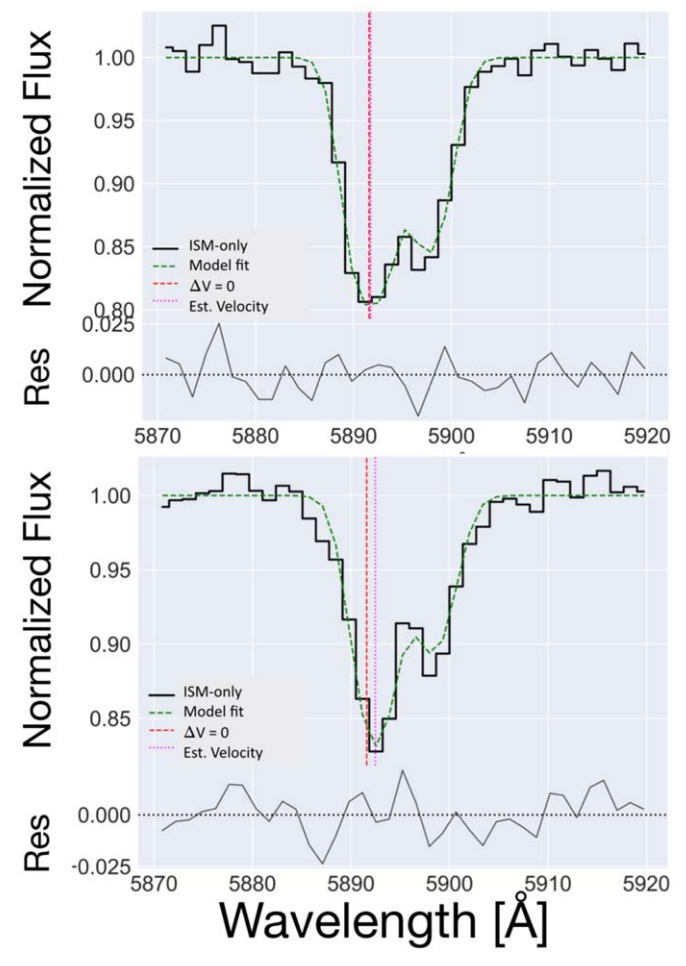


**Figure 6.** The two panels show the modeling of continuum-normalized NaD spectra using the Rupke et al. (2005) absorption model for two different spaxels of a red geyser (MaNGA ID: 1-217022). The observed spectra are shown in black, the best-fit models in green, and the wavelengths corresponding to the estimated velocities in magenta. The bottom subpanels below the main plots show the residuals of the fits.

fraction = 0.2. These parameter values are obtained by fitting the observed NaD ISM spectra for the same galaxy with the same Rupke et al. (2005) model. Mock spectra are created for five assumed input velocity offsets (-100 km s<sup>-1</sup>, -50 km s<sup>-1</sup>, 0 km s<sup>-1</sup>, 50 km s<sup>-1</sup>, and 100 km s<sup>-1</sup>) relative to the systemic velocity. We convolve the resultant profile with the instrumental resolution of MaNGA and then add normally distributed noise to the simulated spectra. We perform the above process for different S/N values ranging from 1 to 20 at each input velocity. We fit the resultant spectra and retrieve the model parameters according to the technique described in this subsection and in Section 3.1. Error estimates on the retrieved velocities are obtained by bootstrapping the simulated "data."

The differences between the retrieved and input velocities for different values of S/N are shown in Figure 7 via solid lines. Each colored line represents a different initial velocity offset value. The plot reveals systematic biases that result from our model fitting and velocity retrieval process. We see that a modest positive (redshifted) bias exists, but for S/N > 10 per dispersion element (gray shaded region), similar to the noise level in the NaD spectra used in our analyses, the bias in all cases is less than  $\sim$ 5 km s<sup>-1</sup>. As we show here, this systematic

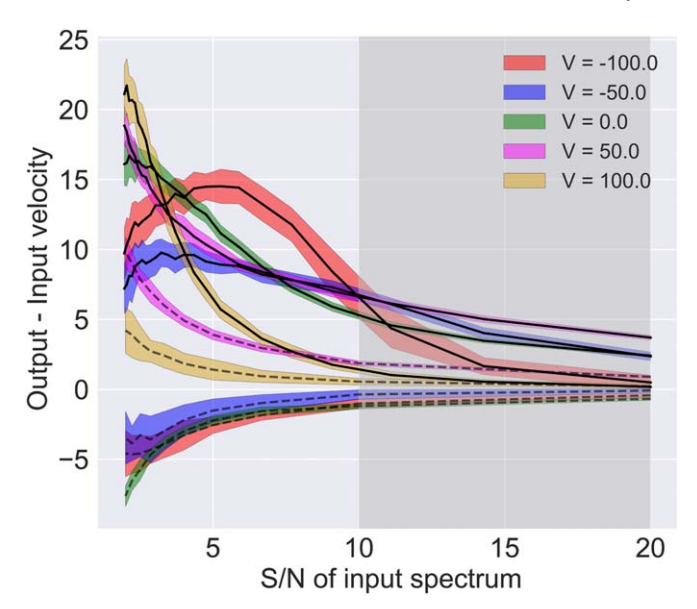


**Figure 7.** Difference between the input velocity (V) of the ISM component used to simulate the mock NaD absorption spectra and the retrieved velocity obtained with our velocity estimation analysis vs. the S/N used in the mock simulation. Each color represents the "true" ISM velocity used for simulating the data. Colored shaded regions depict the  $1\sigma$  error regions on the difference. The solid lines are for realistic sodium doublet absorption profiles while the dashed lines are for doublet profiles that are mirror images of the former. The gray shaded region indicates the S/N in our observed spectrum. This shows the bias in our velocity retrieval process.

error is roughly an order of magnitude smaller than the average velocity offsets we detect in our red geyser samples.

Such a bias probably arises from the combination of the inherent shapes of the subtracted stellar component and the interstellar component of the NaD feature. To check that, we produce similar mock NaD spectra, but this time we reverse the shape of the doublet feature, while keeping the same stellar absorption model. We perform a similar velocity retrieval process and the results are shown as dashed lines in Figure 7. We see that the bias has now switched to the negative side for input velocities <0, and find a much smaller positive bias compared to that in the previous exercise for positive velocities. Varying one or a combination of other parameters like column density, covering fraction, or line width has no impact on the amplitude of the bias.

# 3.4. Stacking Optical Spectra and Interpretation of Stacked Kinematics

In what follows, we are interested in the average behavior of the NaD ISM component across various subsamples as a check on our model fits of spatially binned spectra in individual galaxies. To compute spatially integrated spectra per galaxy, we shift the spectra from each spaxel to the rest frame of the galaxy and continuum-normalize them before co-addition to remove the stellar contribution by the method discussed in Section 3.1. After generating pure-ISM spectra from each spaxel, we construct a circular radius of 8" in each galaxy (which is roughly the angular scale corresponding to the average effective radii of our targets) and include only those spaxels within the radius that satisfy the detection criteria. This is done to remove low-S/N spaxels as well as spaxels near the extreme edge of the IFU. We co-add the spectra and obtain weighted averages, where the weights are the S/N of each

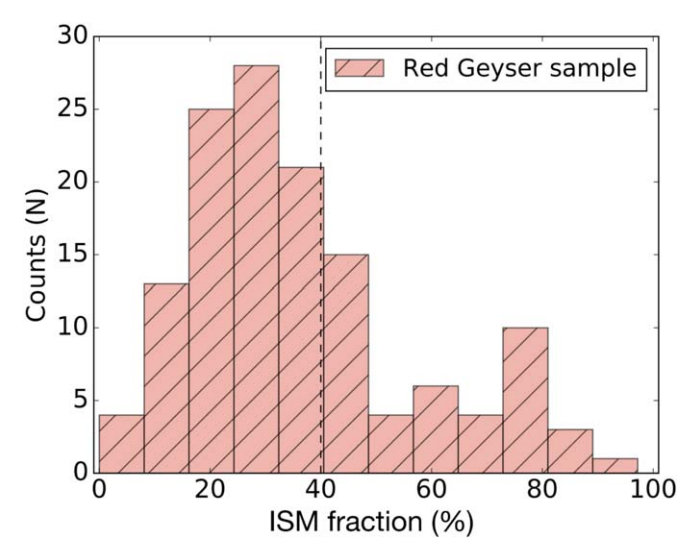


**Figure 8.** The distribution of the mean percentage of ISM contribution in the NaD absorption profile as observed in the red geyser galaxy sample. The dashed line separates red geyser galaxies with ISM fractions >40%, which are greater than twice the typical fraction observed in the control galaxies.

spectrum used in the stacking. The spatially integrated velocity thus obtained represents the average kinematics from the particular galaxy. Once we obtain an integrated spectrum for each galaxy, we also compute a stacked spectrum across each galaxy sample.

# 4. Results

With the ISM component of the NaD absorption spectra extracted, we derive estimates of the EW, column density, and kinematics to search for potential differences between red geysers and normal galaxies. Our four samples of interest comprise 30 radio-detected red geysers (radio-RG), 110 non-radio-detected red geysers (nonradio-RG), 65 radio-detected control sample galaxies (radio-CS), and 393 non-radio-detected control galaxies (nonradio-CS). We will compare these samples to investigate the frequency and strength of ISM NaD absorption in red geysers, both with and without radio AGNs. Finally we will investigate the NaD kinematics.

# 4.1. Fractional Contribution of Interstellar NaD Absorption in Red Geysers

We begin by evaluating the fractional contribution of the ISM component to the total NaD absorption in our sample of 140 red geysers. After fitting the stellar continuum according to the method described in Section 3.1 we calculate the mean EW of the continuum-normalized NaD ISM spectra for each red geyser galaxy by averaging over those spaxels that satisfy the detection test described in Section 3.3. We then compute the ratio of the NaD EW from the ISM component to the total EW derived from the original spectra. The distribution of this ratio for the entire red geyser sample is presented in Figure 8.

Since passive early-type galaxies are dominated by an evolved stellar population, which is the major contributor to the NaD absorption feature, the fraction of ISM component in the NaD EW is generally observed to be low. The fraction is <20% in a majority (80%) of the control galaxies. On the other hand, we find that in 50 out of 140 red geysers (i.e., 35% of the sample), the fractional ISM contribution is >40%, i.e., greater than twice the typical fraction observed in the control galaxies.

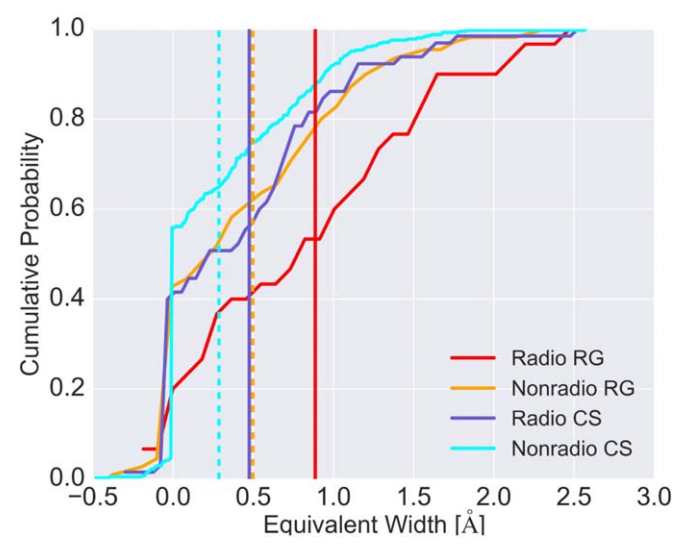


**Figure 9.** Cumulative distribution function showing a comparison of the distribution of the mean NaD ISM EW (computed by averaging over a circular radius of 8") between four different samples—radio-detected red geysers (red), non-radio-detected red geysers (orange), radio-detected control galaxies (blue), and non-radio-detected control galaxies (cyan). The mean of each distribution is shown by same-colored solid (radio-detected galaxies) and dashed (non-radio-detected samples) lines. The radio-detected red geysers show the greatest mean EW of 0.9 Å and a quite different distribution from those of the control samples.

Seventy-seven red geysers (i.e., 55% of the sample) have ISM fractions >30%. If we consider the spatially resolved map for each galaxy, roughly 56% of the red geyser sample show an appreciable presence of ISM gas (i.e., the spaxels satisfy the detection criteria in Section 3.3) over a projected area of  $\ge 5 \times 5 \text{ kpc}^2$ . The fraction increases to 78% if we consider only the radio-detected red geyser sample. This contrasts with the mere 25% for the entire control sample and with 41% for the radio-detected control galaxies.

# 4.2. Comparison of Mean EWs between Radio-detected Red Geysers and Control Sample

Having shown that detections of substantial ISM components are 2–3 times more common among red geysers, we now investigate whether this implies that the total amount of NaDassociated gas, as seen in absorption, is also greater. After removing the stellar contribution, we calculate the column-density-weighted mean NaD EWs across all galaxies in the FIRST-detected radio-RG and nonradio-RG samples and compare them to those of the radio-CS and nonradio-CS galaxies.

The comparison is shown as cumulative distribution functions in Figure 9. The distribution of the NaD EW from the radio-RG galaxies appears to be different from those of both the radio-detected and non-radio-detected control samples. The nonradio-RG sample, however, show a very similar distribution of NaD EWs to the radio-CS sample. We perform a Kolmogorov–Smirnov (K-S) test to measure the statistical significance of the differences of the radio-RG sample from the radio-CS and nonradio-CS samples and find that the null hypothesis that the said distributions are similar is rejected at a level <1% with p values = 0.008 and  $7 \times 10^{-5}$ , respectively. Additionally, the radio red geysers have the highest mean with EW =  $0.9^{+0.31}_{-0.20}$  Å, greater by about 0.45 Å than that of the radio-CS sample, which has a mean EW =  $0.46^{+0.29}_{-0.28}$  Å, and

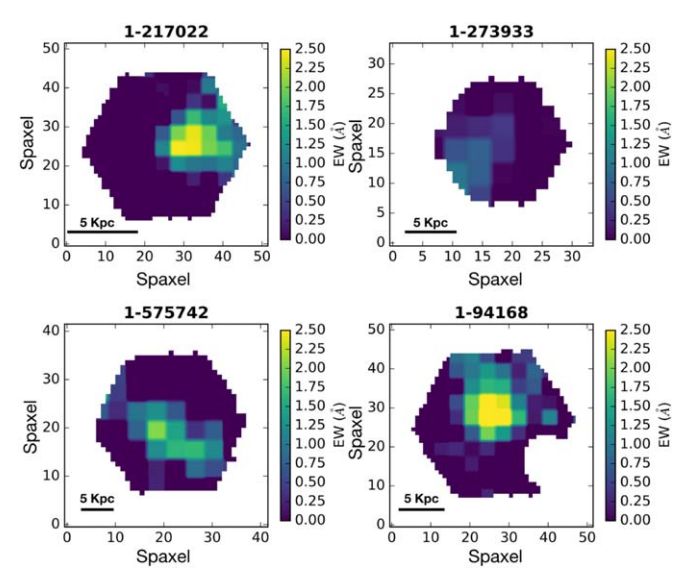


**Figure 10.** Spatially resolved NaD EW maps for four red geysers (MaNGA ID: 1-217022, 1-273933, 1-575742, and 1-94168) derived from the spaxel-wise continuum-normalized NaD spectra for each galaxy. Since the stellar continuum has been factored out, the displayed EW comes entirely from the ISM component. Out of the four red geysers shown here, three are radio-detected (MaNGA ID: 1-217022, 1-273933, and 1-94168).

greater than that of the nonradio-CS sample (EW =  $0.27^{+0.41}_{-0.26}$  Å). The nonradio-RG sample also has a larger NaD EW than both of the control samples with a mean EW =  $0.51^{+0.35}_{-0.33}$  Å. This indicates a greater level of NaD-absorbing material in the ISM of the red geysers generally, but particularly so for the radio-detected sample.

Figure 10 shows the spatially resolved NaD EW maps from the ISM components in four representative red geysers (MaNGA ID: 1-217022, 1-273933, 1-575742, and 1-94168) with ISM contributions  $\frac{\rm EW_{ISM}}{\rm EW_{tot}} > 30\%$ –40%. While all four of them exhibit an ISM NaD enhancement, the EWs in two of them even exceed 2.5 Å in certain regions of these galaxies.

# 4.3. Spatial Extent and Morphology of the NaD Feature

Figure 10 illustrates several common features in the spatial morphology of the ISM NaD distributions observed within the red geysers. These components typically have irregular shapes and are not smooth and symmetric, unlike what is typically expected from the stellar distribution (as in Cazzoli et al. 2014). These asymmetric spatial distributions reinforce the ISM origin of this enhanced NaD absorption.

We have shown that ISM-associated NaD absorption is more common and globally stronger in red geysers, but we can also characterize the typical density distributions of this absorption to distinguish between dense but relatively concentrated components and those that are more extended and diffuse. To quantify the spatial morphology and extent of NaD absorption in each galaxy, we convert the number of spaxels comprising the NaD enhancements in each galaxy to the on-sky projected area using the following conversions:

$$A_{\text{flow}} = A_{\text{NaD}} = N \times (S_{\text{p}})^2 \tag{5}$$

$$A_{\rm gal} = \pi R_{\rm e}^2 \left( b/a \right) \tag{6}$$

where N is the number of spaxels;  $S_p$  is the pixel scale, which is 0."5 for MaNGA;  $R_e$  indicates the effective radius of the

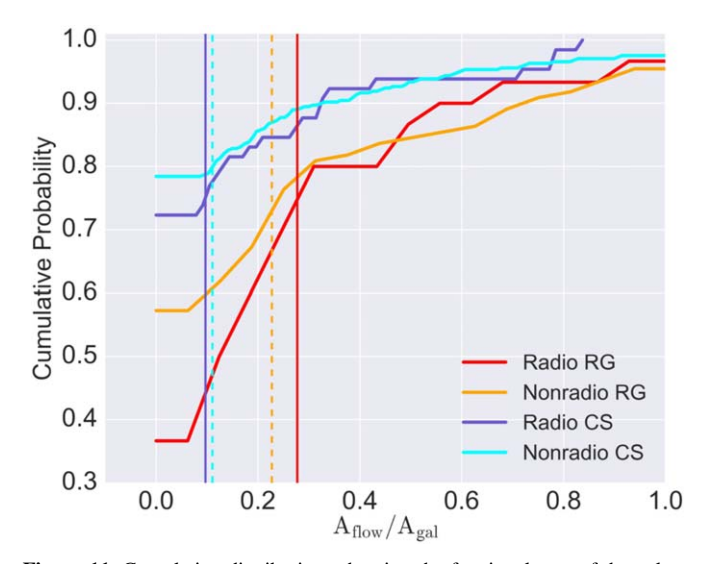


**Figure 11.** Cumulative distributions showing the fractional area of the galaxy comprising cooler neutral ISM gas via NaD absorption for radio-detected and non-radio-detected red geysers (red and orange, respectively) and control sample galaxies (blue and cyan, respectively). The radio-detected red geysers cover, on average, the largest fractional area of NaD absorption (red solid line), almost three times larger than that of the mean of the radio-detected control sample (blue solid line).

galaxy; and b/a gives the axis ratio. Hence the quantity  $A_{\rm flow}/A_{\rm gal}$  gives the fractional area covered by the NaD ISM absorption as compared to the on-sky projected area of the entire galaxy. Figure 11 shows the cumulative distributions of this fraction for radio-RG, nonradio-RG, radio-CS, and nonradio-CS galaxies. We see that when ISM NaD absorption above our threshold is detected, it covers a wider fractional area  $(0.28^{+0.09}_{-0.07})$  within the average radio-detected red geyser sample compared to its areal fractions— $0.09^{+0.15}_{-0.09}$  and  $0.1^{+0.1}_{-0.09}$ —in the radio-detected and non-radio-detected control samples, respectively. This is consistent with Rupke et al. (2021), where the percentage of galaxy disk area showing inflows/outflows via NaD signatures is found to be within 10%-25% for a sample of Seyfert galaxies. A K-S test reveals that the distribution of fractional area from the radio-RG sample is similar to that from the nonradio-RG sample (p value = 0.161) but differs significantly from those from the radio-CS  $(p = 5 \times 10^{-4})$  and nonradio-CS  $(p = 1 \times 10^{-5})$  galaxies. Here, a p value < 0.01 indicates the null hypothesis of the distributions being similar is rejected at a level <1%. If we define a column density threshold of  $\log N(\text{Na\,I})/\text{cm}^{-2} > 12.3$ , which corresponds to the average NaD column density across the entire red geyser and control samples, we find that 63% of the radio-RG sample show NaD absorption that covers at least 10% of the on-sky projected area in the galaxy. This contrasts with 42% in the nonradio-RG sample and with 27% and 21% in the radio-CS and nonradio-CS galaxies, respectively. Thus, the spatial extent of the cool gas present in the FIRST-detected radio-enhanced red geysers far exceeds that in the other samples of galaxies.

# 4.4. Spatially Resolved NaD Kinematics

By a number of measures, the previous sections have illustrated that red geysers, in particular radio-detected red geysers, feature more prominent levels of ISM-associated cool

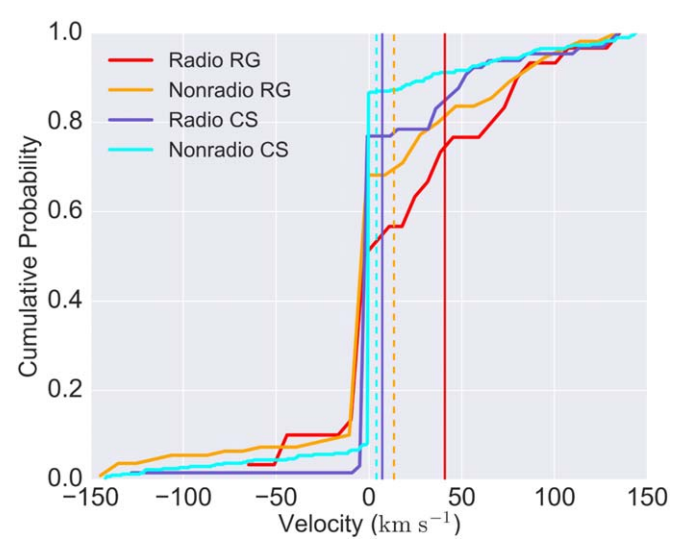


**Figure 12.** The cumulative distribution of the mean velocities obtained from the spatially resolved NaD kinematics for the red geyser and control samples, split by radio detection. The color scheme is the same as that in Figure 9. The mean velocities are calculated by computing the average of the spatially resolved velocities over a circular radius of 8". Both the radio-detected and non-radio-detected red geyser samples show a clear excess in redshift or a positive velocity compared to the control samples.

material as traced by NaD. We now turn to the kinematics of this material as a way to probe its physical origin and evolution. We first calculate the spatially resolved kinematics of the cool neutral ISM in the red geyser and control samples by measuring the Doppler shift of the ISM component of the NaD absorption line with respect to the systemic velocity for each spaxel in every galaxy (see Section 4.2).

We calculate the mean Doppler velocity offset within each galaxy after weighting by the column density, similar to the computation of the mean EW. A comparison of the mean velocities in the radio-detected and non-radio-detected red geysers with those in the control samples (split by radio detection) is shown in Figure 12. The radio-RG sample shows an average positive (or redshifted) velocity  $V = 41 \pm 14 \,\mathrm{km \, s}^{-1}$ , with respect to the systemic velocity. The nonradio-RG sample also shows a positive velocity, though of lesser amplitude, with a mean value of  $13 \pm 9$  km s<sup>-1</sup>. The radio-detected and non-radiodetected control galaxies, on the other hand, have average  $V = 8 \pm 12 \,\mathrm{km \, s^{-1}}$  and  $4 \pm 11 \,\mathrm{km \, s^{-1}}$ , respectively. Thus the radio red geyser sample shows a more significantly redshifted velocity on average. Looking at the statistics across the samples, we find that 86% of the radio-RG sample has  $V \ge 0$ , while only 24% and 13% of the radio-CS and nonradio-CS galaxies show a redshifted velocity. The radio-RG sample shows a statistically different distribution from the radio-detected and non-radiodetected control samples from a K-S test with p values = 0.009 and  $6 \times 10^{-4}$ , respectively. The nonradio-RG sample however shows a similar distribution to radio-CS with p > 0.01, but a significant difference from nonradio-CS (p value =  $1 \times 10^{-3}$ ).

Figure 13 shows spatially resolved velocity maps of the NaD ISM absorption spectra of the four red geysers in Figure 10 (MaNGA ID: 1-217022, 1-273933, 1-575742, and 1-94168). Except for the galaxy in the lower left panel, all are radio-detected. The radio-detected red geysers show significantly redshifted spaxels, generally clustered on one side of the galaxy.

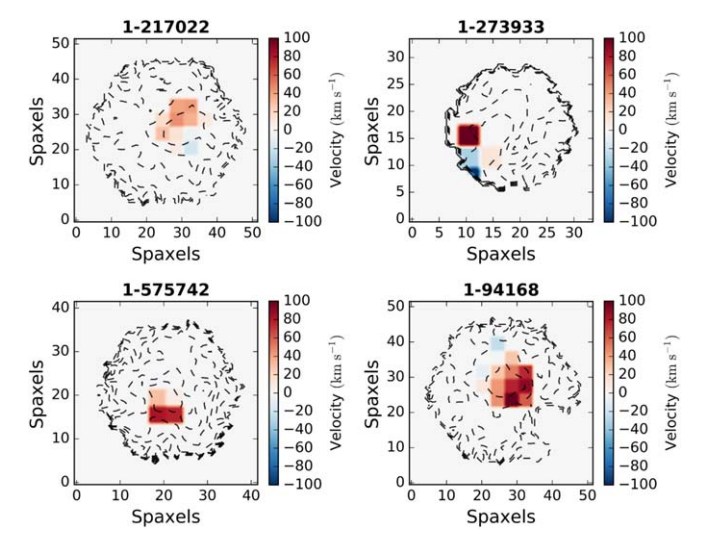


**Figure 13.** Spatially resolved NaD velocity maps of the four red geysers in Figure 10 (MaNGA ID: 1-217022, 1-273933, 1-575742, and 1-94168). The velocities are extracted from modeling of the NaD absorption spectra with the Rupke et al. (2005) model, wrapped in an MCMC framework.

#### 4.5. Global Stacked Kinematics

We have found a clear, redshifted signature (positive velocity,  $V=41~\rm km~s^{-1}$ ) in the average of the spatially resolved NaD offset velocity in the radio-detected red geyser galaxies. However, to estimate these average velocities, we perform Bayesian fitting assuming a specific absorption model to each spaxel (Section 3.3) and compute the mean velocities after weighting by column density. We have shown in Figure 7 that a small but positive bias ( $\leq 5~\rm km~s^{-1}$  at S/N > 10 per dispersion element) can emerge from the fitting algorithm used for the kinematic analyses. Thus to ensure that the velocities we get do not arise from artifacts of model fitting or averaging, we compute the kinematics of stacked NaD profiles from all four samples of galaxies to check if we will see similar trends.

We only use spaxels that meet the criteria described in Section 3.3. Additionally we impose another constraint that the considered spaxels should have a measured EW of the total NaD feature (including both stellar and ISM contributions) of >2 Å. This picks out spaxels with an appreciable NaD signal in each galaxy and provides confidence in the measured EW from the spectra. We then perform a spaxel-wise stacking of the continuum-normalized spectra around the NaD feature and over each sample. The stacked spectra for all four samples are shown in Figure 14. The red geyser samples feature a positive velocity offset. The radio-detected red geysers show a higher redshifted velocity  $(+53 \pm 6 \, \mathrm{km \, s^{-1}})$  compared to the non-radio-detected geysers  $(31 \pm 5 \, \mathrm{km \, s^{-1}})$ . The control samples do not show any significant redshift signature relative to the systemic velocity and show values within  $\pm 10 \,\mathrm{km \, s^{-1}}$  with large errors (see Table 1, Column 5). The errors quoted in Table 1 indicate the mean  $1\sigma$ uncertainty over the whole sample. The stacked velocity values agree well with the average resolved kinematic measurements obtained in Section 4.4.

### 5. Discussion

We have examined the cool ISM properties as probed by NaD in four samples of interest: 30 radio-detected red geysers, 110 non-radio-detected red geysers, 65 radio-detected control sample galaxies, and 393 non-radio-detected control sample

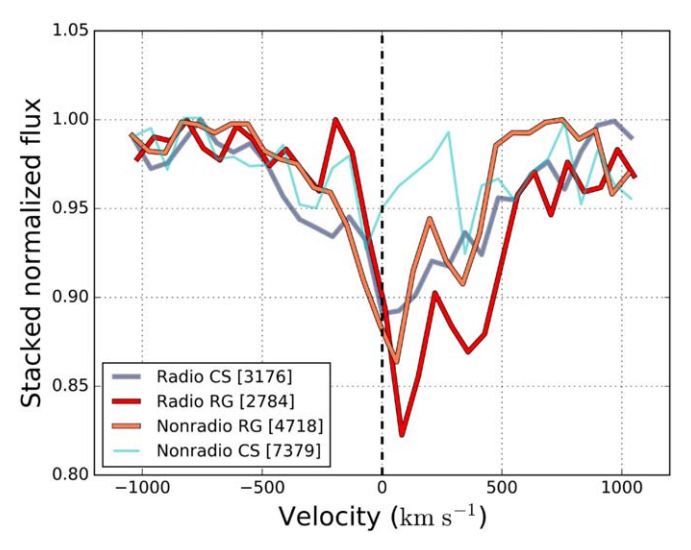


**Figure 14.** Stacked and normalized NaD spectra containing only the ISM component for radio-detected and non-radio-detected red geysers (red and orange, respectively) and control sample galaxies (blue and cyan, respectively). The total number of spaxels with a detected NaD ISM used in the stacking for each of the galaxy samples is mentioned in the legend in square brackets. The radio-detected red geyser sample shows the highest positive velocity (or inflow) relative to the systemic velocity, closely followed by the non-radio-detected geysers. The control samples do not exhibit any visible redshift signature in the stacked sample.

galaxies. Table 1 summarizes the main findings along with the mean  $1\sigma$  error values calculated within each galaxy sample.

We find that the radio-detected red geyser sample shows the largest mean EW  $(0.9\,\text{Å})$  from the NaD ISM component, as compared to the rest of the samples (Table 1, Column 2). Figure 9 shows that the average EW in the radio-RG sample is about 0.5 Å larger than those of the control galaxies, irrespective of radio detection. We also find that 78% of the radio-RG sample possess an appreciable amount of cool gas detected over a projected area  $>5 \times 5\,\text{kpc}^2$ , which is the largest as compared to the other samples. The NaD in the radio-detected red geysers also occupies a larger on-sky area on average, roughly 28% of the projected area of the galaxy (Figure 11). These results imply that red geyser galaxies, which host low-luminosity radio AGNs, typically have an abundant supply of cool gas. A rough estimate of the mass of this detected cool gas is given later in this discussion in Section 5.1.

Figure 12 shows that the average Doppler shift of NaD obtained from the spatially resolved kinematics in the radio-RG sample is roughly  $40 \,\mathrm{km} \,\mathrm{s}^{-1}$  with respect to the systemic velocity. The nonradio-RG sample shows a lower positive velocity of 13 km s<sup>-1</sup>. The control galaxies, irrespective of radio detection, show almost zero velocity within the uncertainties (Table 1). This result very closely matches the global stacked kinematics obtained by stacking all the galaxies in each of the four samples. We find that the radio-detected red geysers show a strong redshift or positive velocity of about 53 km s<sup>-1</sup> compared to the other samples (Figure 14, also see Table 1). Redshift in absorption indicates gas inflowing toward the galaxy, away from the observer. The correlation with radio properties together with the inflowing kinematics possibly indicates that the cool gas is fueling the central AGN in the radio-detected red geyser galaxies, very similar to the prototypical red geyser in Cheung et al. (2016). It is interesting that the radio-detected control galaxy sample also displays a moderate amount of ISM-associated cool gas via NaD

absorption (mean EW =  $0.46\,\text{Å}$ ) but shows no inflowing signature as in the red geysers. Our interpretation in alignment with Roy et al. (2018) is that these radio-detected control galaxies, which also host low-luminosity radio AGNs, are not capable of driving energetic winds like red geysers in the present time but they might in the future. This detected cool gas may slowly accumulate over time and can eventually fuel the central AGN, which can then trigger the red geyser winds.

# 5.1. Cool Gas Mass and Inflow Rates

In order to get a rough estimate of the implied mass inflow rate in red geysers, we adopt the following equation from Roberts-Borsani & Saintonge (2019):

$$\dot{M}_{\text{out}} = \Omega \,\mu \,m_{\text{H}} \,N(\text{H}) \,v \,r \tag{7}$$

where  $\Omega$  is the solid angle subtended by the wind at its origin,  $m_{\rm H}$  is the mean atomic weight (with a  $\mu=1.4$  correction for the relative He abundance),  $N({\rm H})$  is the column density of hydrogen along the line of sight, v is the Doppler velocity, and r is the extent of NaD absorption in the galaxy with respect to the center.

Making the same assumptions as Rupke et al. (2005), the column density of hydrogen can be written as

$$N(H) = \frac{N(\text{Na I})}{\chi(\text{Na I}) d(\text{Na I}) Z(\text{Na I})}$$
(8)

where  $N({\rm Na\,I})$  is the sodium column density,  $\chi({\rm Na\,I}) = N$  (Na I)/ $N({\rm Na\,I})$  is the assumed ionization fraction,  $d({\rm Na\,I})$  is the fraction depletion onto dust, and  $Z({\rm Na\,I})$  is the Na abundance. We assume a 90% ionization fraction ( $\chi({\rm Na\,I}) = 0.1$ ), a Galactic value for the depletion onto dust (log  $d({\rm Na\,I}) = -0.95$ ), and solar metallicity ( $Z_{\rm solar}({\rm Na\,I}) = \log[N({\rm Na\,I})/N({\rm H})] = -5.69$ ) similar to that assumed in Rupke et al. (2005). Putting the log  $N({\rm Na\,I})$  [cm $^{-2}$ ] values (which range from 11.6 to 13.7) obtained from modeling the NaD absorption feature in the radio-detected red geyser sample, we obtain an average log  $N({\rm H})/{\rm cm}^{-2} \sim 19.50$ –21.30. This is roughly in agreement with the log  $N({\rm H})/{\rm cm}^{-2} \sim 21$  estimated according to Bohlin et al. (1978) from the average dust extinction in similar galaxies.

With these assumptions and setting  $\Omega vr$  in Equation (7) equal to  $C_{\rm f}A_{\rm NaD}/t_{\rm acc}$ , where  $A_{\rm NaD}$  is the on-sky projected area of the galaxy comprising NaD absorption from Section 4.3 and  $t_{\rm acc}$  is the accretion timescale  $\sim \frac{R_{\rm e}}{v}$ , we get

$$\dot{M}_{\text{out}} = \mu \, m_{\text{H}} \, C_{\text{f}} \, N(\text{H}) \, A_{\text{NaD}} \, \frac{\nu}{R}. \tag{9}$$

The total mass of the gas can be estimated by the assumption  $M_{\rm tot} = \dot{M}_{\rm out} \times t_{\rm acc}$ :

$$M_{\text{tot}} = \mu \, m_{\text{H}} \, C_{\text{f}} \, N(\text{H}) \, A_{\text{NaD}}. \tag{10}$$

The cloud covering factor  $C_{\rm f}$  is taken to be 0.4, the average value obtained from our model fits. For the radio-detected red geysers, the NaD velocity  $(\nu)$  varies from  $10~{\rm km~s}^{-1}$  to  $100~{\rm km~s}^{-1}$  (Figure 12) with a mean of  ${\sim}45~{\rm km~s}^{-1}$  (Table 1, Columns 4 and 5). The estimated total mass ranges from  $M_{\rm cool} \sim 0.1 \times 10^7 \, M_{\odot}$  to  $5 \times 10^8 \, M_{\odot}$  within the radio-detected red geyser sample while the mass inflow rate spans a large range  ${\sim}0.02-5\, M_{\odot}~{\rm yr}^{-1}$ . The estimated hydrogen column density, the mass flow rates, and the mass of the gas for each

Table 1
Summary of the NaD ISM Properties Obtained for the Four Galaxy Samples

Sample	Mean EW (Å)	Fractional Area On-sky	Mean Resolved V (km s <sup>-1</sup> )	Stacked V (km s <sup>-1</sup> )
Radio red geysers	$0.90^{+0.31}_{-0.30}$	$0.28^{+0.09}_{-0.07}$	$40.86 \pm 14.07$	$52.8 \pm 6.27$
Non-radio red geysers	$0.51^{+0.35}_{-0.33}$	$0.22^{+0.15}_{-0.13}$	$13.56 \pm 9.21$	$31.0\pm5.02$
Radio control sample	$0.46^{+0.29}_{-0.28}$	$0.09^{+0.15}_{-0.09}$	$8.13 \pm 12.10$	$10.2\pm7.78$
Non-radio control sample	$0.27^{0.41}_{-0.26}$	$0.1^{+0.1}_{-0.09}$	$4.00\pm11.97$	$-28.1\pm25.3$

 Table 2

 Estimated Mass and Inflow Rate of Cool Gas for the Radio-detected Red Geyser Galaxies

MaNGA ID	<b>Radio Luminosity</b> $L (10^{22} \text{ W Hz}^{-1})$	<b>Hydrogen Column Density log</b> N(H) (cm <sup>-2</sup> )	Inflow Rate $(M_{\odot} \text{ yr}^{-1})$	Gas Mass $(10^8 M_{\odot})$
1-352569	8.79	$20.45 \pm 1.51$	$0.19 \pm 0.02$	$2.4 \pm 0.21$
1-23958	0.32	$20.89 \pm 0.45$	$0.47 \pm 0.03$	$1.3 \pm 0.10$
1-113668	5.92	$20.38 \pm 2.12$	$-0.41 \pm 0.04$	$3.5 \pm 0.36$
1-595166	3.19	$20.52 \pm 1.99$	$-0.78 \pm 0.04$	$2.5 \pm 0.13$
1-550578	7.81	$20.28 \pm 1.73$	$-0.23 \pm 0.01$	$0.96 \pm 0.10$
1-634825	1.26	$21.20 \pm 0.28$	$1.71 \pm 0.22$	$4.3 \pm 0.26$
1-37036	0.12	$20.03 \pm 2.07$	$0.02 \pm 2 \times 10^{-3}$	$0.03 \pm 5 \times 10^{-3}$
1-43718	1.15	$20.32 \pm 1.20$	$0.05 \pm 9 \times 10^{-3}$	$0.13 \pm 0.02$
1-218116	2.06	0.0	0.0	0.0
1-217022	0.16	$21.27 \pm 0.14$	$0.46 \pm 0.12$	$2.4\pm0.18$
1-256446	2.29	$20.81 \pm 0.60$	$1.80 \pm 0.10$	$1.9\pm0.22$
1-94168	0.52	$21.11 \pm 0.27$	$1.22 \pm 0.08$	$3.7 \pm 0.24$
1-209926	3.36	$20.68 \pm 0.24$	$0.78 \pm 0.07$	$5.1 \pm 0.48$
1-273933	2.46	$20.47 \pm 0.96$	$-0.03 \pm 0.02$	$0.3 \pm 0.04$
1-245451	5.78	$21.07 \pm 0.14$	$5.67 \pm 0.22$	$5.9 \pm 0.62$
1-198182	1.30	0.0	0.0	0.0
1-210863	0.95	$19.48 \pm 5.46$	$0.01 \pm 5 \times 10^{-3}$	$0.01 \pm 3 \times 10^{-3}$
1-289864	77.52	0.0	0.0	0.0
1-24104	0.36	$20.53 \pm 1.54$	$0.38 \pm 0.02$	$0.7 \pm 0.02$
1-378770	45.32	$20.49 \pm 0.51$	$0.88 \pm 0.06$	$3.3 \pm 0.42$
1-279073	0.54	$20.04 \pm 1.05$	$0.01 \pm 3 \times 10^{-3}$	$0.02 \pm 5 \times 10^{-3}$
1-188530	8.37	$20.37 \pm 0.93$	$3.21 \pm 0.2$	$3.9 \pm 0.05$
1-209772	23.84	$20.10 \pm 3.99$	$2.8 \pm 0.5$	$3.2 \pm 0.66$
1-268789	6.51	$20.19 \pm 0.81$	$0.04 \pm 0.01$	$1.0 \pm 0.02$
1-567948	0.13	$19.90 \pm 2.32$	$0.4 \pm 0.1$	$2.1 \pm 0.3$
1-96290	6.22	$20.27 \pm 1.50$	$0.27 \pm 0.03$	$2.0\pm0.24$
1-37440	0.06	$20.9 \pm 0.55$	$2.38 \pm 0.01$	$1.1 \pm 0.04$
1-321221	0.25	0.0	0.0	0.0
1-322336	5.64	$20.62 \pm 0.31$	$0.35 \pm 0.06$	$2.3 \pm 0.40$
1-627331	0.91	0.0	0.0	0.0

galaxy in the radio-RG sample are given in Table 2 along with their  $1\sigma$  uncertainties. The  $1\sigma$  errors in the column density are derived from MCMC fitting of the absorption line model (Section 3.3) to the observed NaD spectrum in each spaxel satisfying the detection criteria within each galaxy and adding them in quadrature. The corresponding errors in flow rate and gas mass are obtained from simple error propagation.

A few galaxies show negative velocity (or blueshift) indicating possible outflowing gas and the outflow rate, also estimated from Equation (9), is given with a negative sign in the table. As expected, the majority of radio-detected red geysers show inflowing gas. Those galaxies with no NaD ISM component detected in any spaxels (following Section 3.3) are tabulated as having zero inflow rate and  $M_{\rm tot}$  although there may be cool gas present below our detection level.

# 5.2. Origin of Inflowing Gas

Infalling gas in red geysers at the estimated accretion rates can come from a variety of sources:

- 1. Accretion from outside the galaxy and its halo. Galaxy mergers, specifically minor mergers, present an obvious mechanism (Sanders et al. 1988; Kaviraj 2014; Pace & Salim 2014; Weston et al. 2017; Martin et al. 2018).
- 2. A completely internal source, such as gas injected into the ISM during stellar mass loss (Conroy et al. 2015) that undergoes cooling and condensation, perhaps eventually feeding an AGN (Ciotti & Ostriker 1997, 2001, 2007).
- 3. A fountain scenario, where warm ionized outflowing gas, driven out by the central AGN from earlier geyser episodes, rises into the halo, cools and condenses as it expands, and then falls back onto the galaxy (e.g., Shapiro & Field 1976; Bregman 1980; Norman & Ikeuchi 1989; Tremblay et al. 2016, 2018; Voit et al. 2017).

Numerous observations have measured the merger rates in nearby galaxies (see Ellison et al. 2015 and references therein) and several authors have emphasized widespread merger activity when observational evidence sensitive to long timescales and low mass ratios is scrutinized (e.g., van Dokkum 2005; Sancisi et al. 2008). For galaxies with stellar masses between 1010.5 and  $10^{12} M_{\odot}$ , the average predicted merger rate per galaxy (assuming typical mass ratios of minor mergers ~1:10) from semiempirical models and hydrodynamical simulations is roughly 0.1 Gyr (Hopkins et al. 2010; O'Leary et al. 2021). Thus galaxy mergers with a 1:10 (or greater) mass ratio can generate an  $M_*$  accretion rate of  $\frac{0.1 \times 0.1 \times 1. \times 10^{11} M_{\odot}}{10^{9} \text{ yr}} = 1 M_{\odot} \text{ yr}^{-1}$  on average. If 10% of rate of  $\frac{10^9 \text{ yr}}{10^9 \text{ yr}} = 1 M_{\odot} \text{ yr}$  on average. If 10% of this value lies in cold gas, the estimated accretion rate is roughly  $0.1 \, M_{\odot} \, \text{yr}^{-1}$ . This is similar to the accretion rates quoted in Capelo et al. (2015), who performed detailed simulations by exploring a wide merger parameter space including different initial mass ratios, orbital configurations, and gas fractions with high spatial and temporal resolution. The average cool gas inflow rate we estimate from NaD in red geysers is similar to the accretion rate implied by minor mergers. Merging gas-rich dwarfs may therefore be important sources of infalling gas. The apparently higher detection rate of NaD-associated inflows in red geysers compared to that of control sample galaxies may be telling us that red geysers are a signpost of accretion activity. Indeed, some red geysers in our sample with accretion rates  $\sim 5 \, M_{\odot} \, \mathrm{yr}^{-1}$  may be signaling a peak in the instantaneous accretion rate during a merger event.

In addition to mergers, Ciotti et al. (1991) and Ciotti & Ostriker (2007) predicted that a significant amount of gas,  $\sim 20\%-30\%$  of the initial stellar mass of the galaxy, is donated throughout the galaxy over the course of stellar evolution and supernova explosions. This gas can be accreted onto an AGN. The radiative cooling time of this warm gas in typical elliptical galaxies is roughly  $10^{7.5-8}$  yr. Ciotti & Ostriker (2007) quoted a mass return rate of  $\sim 5-10\,M_\odot$  yr $^{-1}$  from the stellar populations over the cooling timescale, which exceeds the cool gas inflow rates we observe in red geysers. Moreover, some fraction of warm ionized gas ( $M \sim 10^{5-6}\,M_\odot$ ) ejected by red geyser winds may accumulate within the ISM or the circumgalactic medium of the galaxies over time. After cooling and condensation, this material might also become a source for the observed inflows.

Considering the different sources of infalling gas discussed above, we have found from visual inspection that most of the radio-detected red geysers show a spatially irregular and clumpy NaD distribution (see Figure 10). Additionally, we see from Figure 11 that the average fractional area occupied by NaD absorption is around 30% of the projected area of the entire galaxy for the radio red geyser sample, which implies a concentrated, lumpy distribution of gas confined in a small region. The recycled gas from the fountain scenario might be expected to present a more diffuse and smooth component than is observed here.

Cooling ISM gas originating from stellar winds and supernovae might also be expected to cover a larger area of the whole galaxy. Moreover, cool gas originating from stars might show greater correlations with the stellar kinematics, which are not observed here.

It is also interesting to consider the relatively short timescales of dust-enshrouded cool gas. As discussed in Rowlands et al. (2012), dust in early-type galaxies gets destroyed on relatively short timescales, ranging from 50 to 500 Myr, due to thermal sputtering from the hot X-ray halo surrounding the ISM or from shocks generated from Type Ia supernovae. The signatures of clumpy, dust-associated NaD gas are likely short-lived, suggesting stochastic inflow episodes

from merging systems over a more continuous "rain" of recycled material.

Finally, we note that the detected cool gas in red geysers, with masses ranging from  $10^7$  to  $10^8 \, M_\odot$  and average accretion rates  $\sim 0.1-5 \, M_\odot \, {\rm yr}^{-1}$ , might be expected to trigger an SFR of at least  $1 \, M_\odot \, {\rm yr}^{-1}$ . However, the observed average SFR ( $\sim 10^{-2} \, M_\odot \, {\rm yr}^{-1}$ ) is several orders of magnitude lower, as evident from Figure 1. This again is suggestive of active feedback mechanisms, perhaps related to the red geyser winds themselves, that are effective in suppressing star formation in these galaxies.

### 6. Conclusion

We have performed a set of analyses of the sodium doublet absorption feature as a tracer of cool ISM gas in red geyser galaxies and a matched control sample using spatially resolved data from the SDSS-IV MaNGA survey. After carefully subtracting the stellar contribution, we find an excess in NaD absorption, which we ascribe to the presence of cool material in the ISM. We study the properties of this gas in our radio-detected red geyser sample (30 galaxies) and compare them to those in several other samples—namely, 110 non-radio-detected red geysers and 65 radio-detected and 393 non-radio-detected control samples.

We measure the kinematic behavior of the cool gas by computing the average velocity offsets in spatially resolved maps, the integrated offsets per galaxy, and the stacked kinematics of ISM NaD spectra across all four galaxy samples. We find that the NaD in the radio-detected red geysers shows a clear redshift (40–50 km s $^{-1}$ ) with respect to the systemic velocity. We interpret this result as an indication that the cool gas is inflowing into the galaxy center. The non-radio-detected sample of red geysers show a similar redshift, but of slightly smaller amplitude on average ( $\sim$ 15–30 km s $^{-1}$ ). The control samples however show average velocity offsets that are around zero or slightly negative (<10 km s $^{-1}$ ).

In order to check that the observed redshift is robust due to the systematics of the fitting technique itself, we test our fitting approach using simulated spectra of varying S/N and different input velocities (Figure 7). We find that at the S/N of our observation (>10 per dispersion element), there exists a modest systematic bias of  $\leq$ 5 km s<sup>-1</sup>, which is, however, much smaller than the velocity inflow values we observe.

The accretion of cool gas inflowing into the center coupled with the radio enhancement in the radio red geyser sample indicates that the central low-luminosity radio AGN is possibly fueled by the cool neutral gas clouds in the ISM. Both external sources (like mergers) and internal processes (stellar mass loss and accumulation of gas from relic geyser winds) can explain the observed accretion rates, which span a vast range  $\sim 0.02-5\,M_\odot\,{\rm yr}^{-1}$  with an estimated total mass of the cool gas of  $\sim 10^7-10^8\,M_\odot$ . Although this gas is capable of triggering an easily detectable level of star formation ( $\sim 1\,M_\odot\,{\rm yr}^{-1}$ ), the observed quiescent nature of the red geysers with an SFR almost two orders of magnitude lower indicates evidence of maintenance-mode feedback in action and possibly associated with the red geyser phenomenon itself.

The authors thank the anonymous referee for helpful comments and suggestions that significantly improved the manuscript. This research was supported by the National Science Foundation under award No. 1816388. R.R. thanks the Brazilian

funding agencies CNPq, CAPES, and FAPERGS. Funding for SDSS-IV has been provided by the Alfred P. Sloan Foundation, the U.S. Department of Energy Office of Science, and the participating institutions. SDSS-IV acknowledges support and resources from the Center for High-performance Computing at the University of Utah. The SDSS website is www.sdss.org.

SDSS-IV is managed by the Astrophysical Research Consortium for the Participating Institutions of the SDSS Collaboration including the Brazilian Participation Group, the Carnegie Institution for Science, Carnegie Mellon University, the Chilean Participation Group, the French Participation Group, the Harvard-Smithsonian Center for Astrophysics, Instituto de Astrofísica de Canarias, the Johns Hopkins University, Kavli Institute for the Physics and Mathematics of the Universe/University of Tokyo, the Korean Participation Group, Lawrence Berkeley National Laboratory, Leibniz Institut für Astrophysik Potsdam, Max-Planck-Institut für Astronomie (Heidelberg), Max-Planck-Institut für Astrophysik (Garching), Max-Planck-Institut für Extraterrestrische Physik, the National Astronomical Observatories of China, New Mexico State University, New York University, University of Notre Dame, Observatário Nacional/MCTI, the Ohio State University, Pennsylvania State University, Shanghai Astronomical Observatory, the United Kingdom Participation Group, Universidad Nacional Autónoma de México, University of Arizona, University of Colorado Boulder, University of Oxford, University of Portsmouth, University of Utah, University of Virginia, University of Washington, University of Wisconsin, Vanderbilt University, and Yale University. RAR acknowledges financial support from Conselho Nacional de Desenvolvimento Científico e Tecnológico and Fundação de Amparo à Pesquisa do Estado do Rio Grande do Sul.

### **ORCID iDs**

Namrata Roy https://orcid.org/0000-0002-4430-8846
Kevin Bundy https://orcid.org/0000-0001-9742-3138
Kate H. R. Rubin https://orcid.org/0000-0001-6248-1864
Kate Rowlands https://orcid.org/0000-0001-7883-8434
Kyle Westfall https://orcid.org/0000-0003-1809-6920
Dmitry Bizyaev https://orcid.org/0000-0002-3601-133X
David V. Stark https://orcid.org/0000-0002-3746-2853
Rogemar A. Riffel https://orcid.org/0000-0003-0483-3723
Ivan Lacerna https://orcid.org/0000-0002-7802-7356
Xuanyi Wu https://orcid.org/0000-0002-0744-8022
Niv Drory https://orcid.org/0000-0002-7339-3170

### References

```
Ahumada, R., Prieto, C. A., Almeida, A., et al. 2020, ApJS, 249, 3
Alatalo, K., Cales, S. L., Rich, J. A., et al. 2016, ApJS, 224, 38
Albareti, F. D., Allende Prieto, C., Almeida, A., et al. 2017, ApJS, 233, 25
Baldwin, J. A., Phillips, M. M., & Terlevich, R. 1981, PASP, 93, 5
Belfiore, F., Westfall, K. B., Schaefer, A., et al. 2019, AJ, 158, 160
Bryant, J. J., Croom, S. M., van de Sande, J., et al. 2019, MNRAS, 483, 458
Binney, J., & Tabor, G. 1995, MNRAS, 276, 663
Blanton, M. R., Bershady, M. A., Abolfathi, B., et al. 2017, AJ, 154, 28
Bregman, J. N. 1980, ApJ, 236, 577
Roberts-Borsani, G. W., & Saintonge, A. 2019, MNRAS, 482, 4111
Bohlin, R. C., Savage, B. D., & Drake, J. F. 1978, ApJ, 224, 132
Bower, R. G., Benson, A. J., Malbon, R., et al. 2006, MNRAS, 370, 645
Bundy, K., Bershady, M. A., Law, D. R., et al. 2015, ApJ, 798, 7
Capelo, P. R., Volonteri, M., Dotti, M., et al. 2015, MNRAS, 447, 2123
Cappellari, M., & Emsellem, E. 2004, PASP, 116, 138
Cappellari, M. 2017, MNRAS, 466, 798
Cazzoli, S., Arribas, S., Colina, L., et al. 2014, A&A, 569, A14
```

```
Cazzoli, S., Arribas, S., Maiolino, R., et al. 2016, A&A, 590, A125
Chen, Y., Shi, Y., Tremonti, C. a., et al. 2016, NatCo, 7, 13269
Cheung, E., Bundy, K., Cappellari, M., et al. 2016, Natur, 533, 504
Ciotti, L., D'Ercole, A., Pellegrini, S., & Renzini, A. 1991, ApJ, 376, 380
Ciotti, L., & Ostriker, J. P. 1997, ApJL, 487, L105
Ciotti, L., & Ostriker, J. P. 2001, ApJ, 551, 131
Ciotti, L., & Ostriker, J. P. 2007, ApJ, 665, 1038
Ciotti, L., Ostriker, J. P., & Proga, D. 2010, ApJ, 717, 708
Coil, A. L., Weiner, B. J., Holz, D. E., et al. 2011, ApJ, 743, 46
Conroy, C., van Dokkum, P. G., & Kravtsov, A. 2015, ApJ, 803, 77
Croton, D. J., Springel, V., White, S. D. M., et al. 2006, MNRAS, 365, 11
Davis, T. A., Alatalo, K., Bureau, M., et al. 2013, MNRAS, 429, 534
Drory, N., MacDonald, N., Bershady, M. A., et al. 2015, AJ, 149, 77
Duckworth, C., Starkenburg, T. K., Genel, S., et al. 2020, MNRAS, 495, 4542
Eldridge, J. J., Stanway, E. R., Xiao, L., et al. 2017, PASA, 34, e058
Ellison, S. L., Patton, D. R., & Hickox, R. C. 2015, MNRAS, 451, L35
Faber, S. M., Willmer, C. N. A., Wolf, C., et al. 2007, ApJ, 665, 265
Gunn, J. E., Siegmund, W. A., Mannery, E. J., et al. 2006, AJ, 131, 2332
Hopkins, P. F., Bundy, K., Croton, D., et al. 2010, ApJ, 715, 202
Higson, E., Handley, W., Hobson, M., et al. 2019, Statistics and Computing,
  29, 891
Jacoby, G. H., Hunter, D. A., & Christian, C. A. 1984, ApJS, 56, 257
Kaviraj, S. 2014, MNRAS, 440, 2944
Krug, H. B., Rupke, D. S. N., & Veilleux, S. 2010, ApJ, 708, 1145
Lagos, C. P., Crain, R. A., Schaye, Joop, et al. 2015, MNRAS, 452, 3815
Lagos, C., del, P., Davis, T. A., et al. 2014, MNRAS, 443, 1002
Law, D. R., Yan, R., Bershady, M. A., et al. 2015, AJ, 150, 19
Law, D. R., Cherinka, B., Yan, R. B., et al. 2016, AJ, 152, 83
Martin, D. C., Fanson, J., Schiminovich, D., et al. 2005, ApJL, 619, L1
Martin, G., Kaviraj, S., Volonteri, M., et al. 2018, MNRAS, 476, 2801
Morton, D. C. 1991, ApJS, 77, 119
Falcón-Barroso, J., Sánchez-Blázquez, P., Vazdekis, A., et al. 2011, A&A,
  532, A95, 1388
Norman, C. A., & Ikeuchi, S. 1989, ApJ, 345, 372
O'Leary, J. A., Moster, B. P., Naab, T., et al. 2021, MNRAS, 501, 3215
Pace, C., & Salim, S. 2014, ApJ, 785, 66
Putman, M. E., Peek, J. E. G., & Heitsch, F. 2012, in EAS Publications Series,
  ed. M. A. de Avillez, Vol. 56 (Paris: EDP Sciences), 267
Rowlands, K., Dunne, L., Maddox, S., et al. 2012, MNRAS, 419, 2545
Rupke, D. S., Veilleux, S., & Sanders, D. B. 2005, ApJS, 160, 87
Rupke, D. 2018, Galax, 6, 138
Rupke, D. S. N., Thomas, A. D., & Dopita, M. A. 2021, MNRAS, 503, 4748
Rubin, K. H. R., Prochaska, J. X., Koo, D. C., et al. 2014, ApJ, 794, 156
Rubin, K. H. R., Prochaska, J. X., Koo, D. C., et al. 2012, ApJL, 747, L26
Riffel, R. A., Nemmen, R. S., Ilha, G. S., et al. 2019, MNRAS, 485, 5590
Roy, N., Bundy, K., Cheung, E., et al. 2018, ApJ, 869, 117
Roy, N., Bundy, K., Nevin, R., et al. 2021, ApJ, 913, 33
Salim, S., Lee, J. C., Janowiecki, S., et al. 2016, ApJS, 227, 2
Sancisi, R., Fraternali, F., Oosterloo, T., et al. 2008, A&ARv, 15, 189
Sarzi, M., Falcón-Barroso, J., Davies, R. L., et al. 2006, MNRAS, 366, 1151
Sarzi, M., Kaviraj, S., Nedelchev, B., et al. 2016, MNRAS, 456, L25
Sanders, D. B., Soifer, B. T., Elias, J. H., et al. 1988, ApJ, 325, 74
Sato, T., Martin, C. L., Noeske, K. G., et al. 2009, ApJ, 696, 214
Shapiro, P. R., & Field, G. B. 1976, ApJ, 205, 762
Smee, S. A., Gunn, J. E., Uomoto, A., et al. 2013, AJ, 146, 32
Speagle, J. S. 2020, MNRAS, 493, 3132
Skilling, J. 2006, BayAn, 1, 833
Skilling, J. 2004, in XXIV International Workshop on Bayesian Inference and
   Maximum Entropy Methods in Science and Engineering (Jarinu, Brazil,
  July 09–14, 2017), 395
Tremblay, G. R., Combes, F., Oonk, J. B. R., et al. 2018, ApJ, 865, 13
Tremblay, G. R., Oonk, J. B. R., Combes, F., et al. 2016, Natur, 534, 218
Voit, G. M., Meece, G., Li, Y., et al. 2017, ApJ, 845, 80
Tyson, N. D., & Rich, R. M. 1991, ApJ, 367, 547
van Dokkum, P. G. 2005, AJ, 130, 2647
Vazdekis, A., Ricciardelli, E., Cenarro, A. J., et al. 2012, MNRAS, 424, 157
Veilleux, S., Maiolino, R., Bolatto, A. D., et al. 2020, A&ARv, 28, 2
Wake, D. A., Bundy, K., Diamond-Stanic, A. M., et al. 2017, AJ, 154, 86
Westfall, K. B., Cappellari, M., Bershady, M. A., et al. 2019, AJ, 158, 231
Weiner, B. J., Coil, A. L., Prochaska, J. X., et al. 2009, ApJ, 692, 187
Weston, M. E., McIntosh, D. H., Brodwin, M., et al. 2017, MNRAS, 464, 3882
Yan, R., Bundy, K., Law, D. R., et al. 2016, AJ, 152, 197
Yan, R., Chen, Y., Lazarz, D., et al. 2019, ApJ, 883, 175
Chen, Y.-M., Tremonti, C. A., Heckman, T. M., et al. 2010, AJ, 140, 445
Yesuf, H. M., Koo, D. C., Faber, S. M., et al. 2017, ApJ, 841, 83
Yuan, F., & Narayan, R. 2014, ARA&A, 52, 529
```

Zheng, Y., Peek, J. E. G., Werk, J. K., et al. 2017, ApJ, 834, 179